Late Quaternary aggradation and incision in the headwaters of the Yangtze River, eastern Tibetan Plateau, China

Yu, Yang; Wang, Xianyan; Yi, Shuangwen; Miao, Xiaodong; Vandenberghe, Jef; Li, Yiquan; Lu, Huayu

published in
Bulletin of the Geological Society of America
2022

DOI (link to publisher)
10.1130/B35983.1

document version
Publisher's PDF, also known as Version of record

THE GEOLOGICAL SOCIETY OF AMERICA®

Late Quaternary aggradation and incision in the headwaters of the Yangtze River, eastern Tibetan Plateau, China

Yang Yu[1], Xianyan Wang[1,†], Shuangwen Yi[1], Xiaodong Miao[2], Jef Vandenberghe[1,3], Yiquan Li[1], and Huayu Lu[1]
[1]*School of Geography and Ocean Science, Nanjing University, Nanjing 210023, China*
[2]*School of Resource and Environmental Sciences, Linyi University, Linyi 276000, China*
[3]*Department of Earth Sciences, Vrije Universiteit Amsterdam, De Boelelaan 1085, 1081 HV Amsterdam, The Netherlands*

ABSTRACT

River aggradation or incision at different spatial-temporal scales are governed by tectonics, climate change, and surface processes which all adjust the ratio of sediment load to transport capacity of a channel. But how the river responds to differential tectonic and extreme climate events in a catchment is still poorly understood. Here, we address this issue by reconstructing the distribution, ages, and sedimentary process of fluvial terraces in a tectonically active area and monsoonal environment in the headwaters of the Yangtze River in the eastern Tibetan Plateau, China. Field observations, topographic analyses, and optically stimulated luminescence dating reveal a remarkable fluvial aggradation, followed by terrace formations at elevations of 55–62 m (T7), 42–46 m (T6), 38 m (T5), 22–36 m (T4), 18 m (T3), 12–16 m (T2), and 2–6 m (T1) above the present floodplain. Gravelly fluvial accumulation more than 62 m thick has been dated prior to 24–19 ka. It is regarded as a response to cold climate during the last glacial maximum. Subsequently, the strong monsoon precipitation contributed to cycles of rapid incision and lateral erosion, expressed as cut-in-fill terraces. The correlation of terraces suggests that specific tectonic activity controls the spatial scale and geomorphic characteristics of the terraces, while climate fluctuations determine the valley filling, river incision and terrace formation. Debris and colluvial sediments are frequently interbedded in fluvial sediment sequences, illustrating the episodic, short-timescale blocking of the channel ca. 20 ka. This indicates the potential impact of extreme events on geomorphic evolution in rugged terrain.

INTRODUCTION

Rivers play the most active role in shaping the landscape either by erosion or deposition in a source-to-sink system (e.g., Allen, 2008; Sømmé and Jackson, 2013). The river incises or aggrades alternatively through varying discharge, sediment load, and channel slope as a response to tectonic activities, erosional isostasy, climatic fluctuations, and changes in base level (e.g., Maddy et al., 2000; Stokes et al., 2018; Vandenberghe et al., 2018; De Paula and Magalhães, 2020). In addition, rivers in rugged mountains with high relief resulting from the interaction of tectonics and climate, are generally vulnerable to extreme events, such as orographically enhanced catastrophic precipitation that may initiate landslides, rock-falls, and debris flows, potentially leading to cascading dynamic processes and complex fluvial response (e.g., Molnar et al., 1993; Molnar and Houseman, 2013; Srivastava et al., 2008). In such prominent landforms, river damming and dam failure may strongly influence aggradation and incision both in upstream and downstream directions (e.g., Korup and Montgomery, 2008; Hewitt et al., 2008). Such accumulation of sediment load due to damming effects may abrade or protect the underlying channel bedrock in orogenic mountains, which has profound effects on the evolution of large rivers and regional landforms (e.g., Korup et al., 2010b).

Earlier studies concluded that extreme events, such as earthquakes, extreme rainfall, and glacial activities, could lead to damming of rivers or breaking dams in high relief areas (Korup and Tweed, 2007; Fan et al., 2019; Handwerger et al., 2019). Global warming will probably increase the magnitude of climate fluctuations and extreme events, which potentially may cause a series of natural hazards threatening the inhabitants (e.g., Chug et al., 2020). There are plenty of reports about mega-floods or debris flows in the rivers around the Tibetan Plateau (e.g., Chen et al., 2008; Wu et al., 2016; Cook et al., 2018; Liu et al., 2015, 2018, 2019). But internal mechanisms and interplays between tectonics, climate, and extreme events (such as landslides, debris, and rock-falls) in mountains are still obscure and need to be researched at geological timescale.

The geomorphic evolution at the margins of the Tibetan Plateau is controlled by the rapid and remarkable incision of large rivers, e.g., the Jinsha, Mekong, and Nujiang rivers, and intensive landslides, which could be produced by intensified monsoonal rainfall (e.g., Chen et al., 2008; Kong et al., 2009; Henck et al., 2011; Ferrier et al., 2013; Nie et al., 2018; Schanz et al., 2018; Bao et al., 2020; Tao et al., 2020) (Fig. 1). The strong tectonic activities with frequent earthquakes (such as the Yushu, China surface-wave magnitude (Ms) 7.1 earthquake in 2010) (e.g., Zhang et al., 2013) and the high relief indicate that the upper Yangtze River is vulnerable to extreme processes of landslides and debris flows which may block the valley, leading to the breakage of channel connections in its headwaters (e.g., Chen et al., 2008; Bao et al., 2020) (Fig. 1A). Thus, fluvial systems in this area with intensive monsoonal precipitation and active tectonics could provide important archives from which to assess the fluvial response to extreme events.

In this paper, field investigation with description of the sedimentary sequences has been supplemented with optically stimulated luminescence (OSL) dating to establish the terrace sequence and incision rates of the headwaters of the Yangtze River in the eastern Tibetan Plateau as an example of fluvial response to tectonic movement, climate change, and extreme events. More specifically, we report the valley filling and the formation of cut-in-fill terraces during the last deglaciation, as a response to geomorphic processes, climate fluctuations, and extreme events in a tectonically active setting.

Xianyan Wang https://orcid.org/0000-0002-8281-5734

[†]Corresponding author: xianyanwang@nju.edu.cn.

GSA Bulletin; January/February 2022; v. 134; no. 1/2; p. 371–388; https://doi.org/10.1130/B35983.1; 13 figures; 2 tables.
published online 7 May 2021

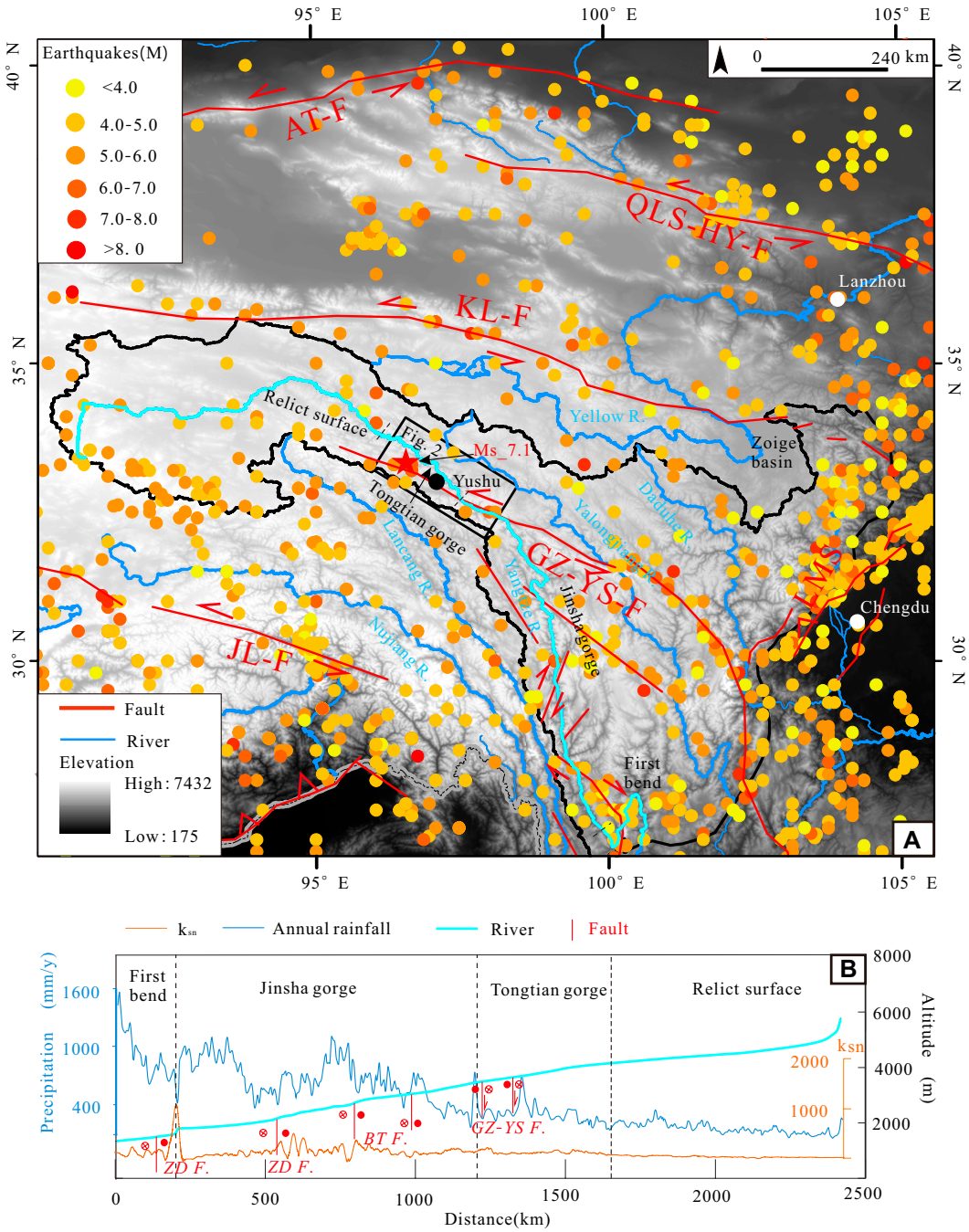

Figure 1. (A) Topographic map of the eastern Tibetan Plateau, China, based on the 90-m digital elevation model from the U.S. National Aeronautics and Space Administration Shuttle Radar Topography Mission, showing the location of rivers, active faults, and historical earthquakes. The Yangtze River is marked by light blue line, while the other rivers are marked by darker blue lines. The black rectangle shows our study area in the headwaters of the Yangtze River. Main strike-slip faults with left-lateral movement are represented from Tapponnier et al. (2001), Deng et al. (2003), and Taylor and Yin (2009). AT-F—Altyn Tagh fault; QLS-HY-F—Qilianshan-Haiyuan fault; KL-F—Kunlun fault; GZ-YS-F—Ganzi-Yushu fault; LMS—Longmenshan; JL-F—Jiali fault. Historical earthquakes from 780 B.C. to 2018 were collected from China Earthquake Networks Center (http://data.earthquake.cn/index.html; M—magnitude). (B) Longitudinal profile of the Yangtze River (light blue), Tropical Rainfall Measuring Mission-derived average annual precipitation (dark blue, http://www.geog.ucsb.edu/~bodo/TRMM/), and normalized channel steepness (ksn, a geomorphic parameter proportional to incision rate; Kirby et al., 2003) (brownish-yellow) along the headwaters of the Yangtze River. Black dash lines divide the river valley into the relict surface, the Tongtian gorge, the Jinsha gorge, and the first bend of the Yangtze River. Left-lateral faults and right-lateral active faults intersecting with the Yangtze River are indicated as GZ-YS-F—Ganzi-Yushu fault; BT-F—Batang fault; ZD-F—Zhongdian fault.

GEOLOGICAL AND GEOGRAPHIC SETTING

The Ganzi-Yushu fault (GZ-YS-F) is a NW-SE strike-slip fault developed due to the lateral extrusion related to the India-Eurasia collision (Fig. 1A). It originates from the Ganzi fault to the southeast and terminates against the Dangjiang fault to the northwest; it is 500 km, tends to the northeast with a dip angle of 70°–85° and coordinates the tectonic activities between the tectonic Qiangtang, Bayankala, and Sichuan-Yunnan blocks of the eastern Tibetan Plateau, China (Wen et al., 2003; Chen et al., 2010; Wu et al., 2012). The GZ-YS-F provides evidence of active transtensional deformation with stream offsets, fault scarps, pull-apart basins, shutter ridges, and earthquakes (Yushu Ms 7.1) since the late Quaternary (Figs. 1A and 2) (e.g., Wen et al., 1985; Zhou et al., 1997; Wen et al., 2003; Wang et al., 2008). Based on the geometry and historical earthquake data, the GZ-YS-F is divided into Ganzi, Manigange, Dengke, Yushu, and Dangjiang segments (e.g., Zhou et al., 1996). This study mainly focuses on the northwestern part of the GZ-YS-F with a series of secondary structures such as folds, normal faults, and thrust faults (Fig. 2). The general slip movement between the Qiangtang and Bayankala blocks led to local fragmentation of the headwaters of the Yangtze

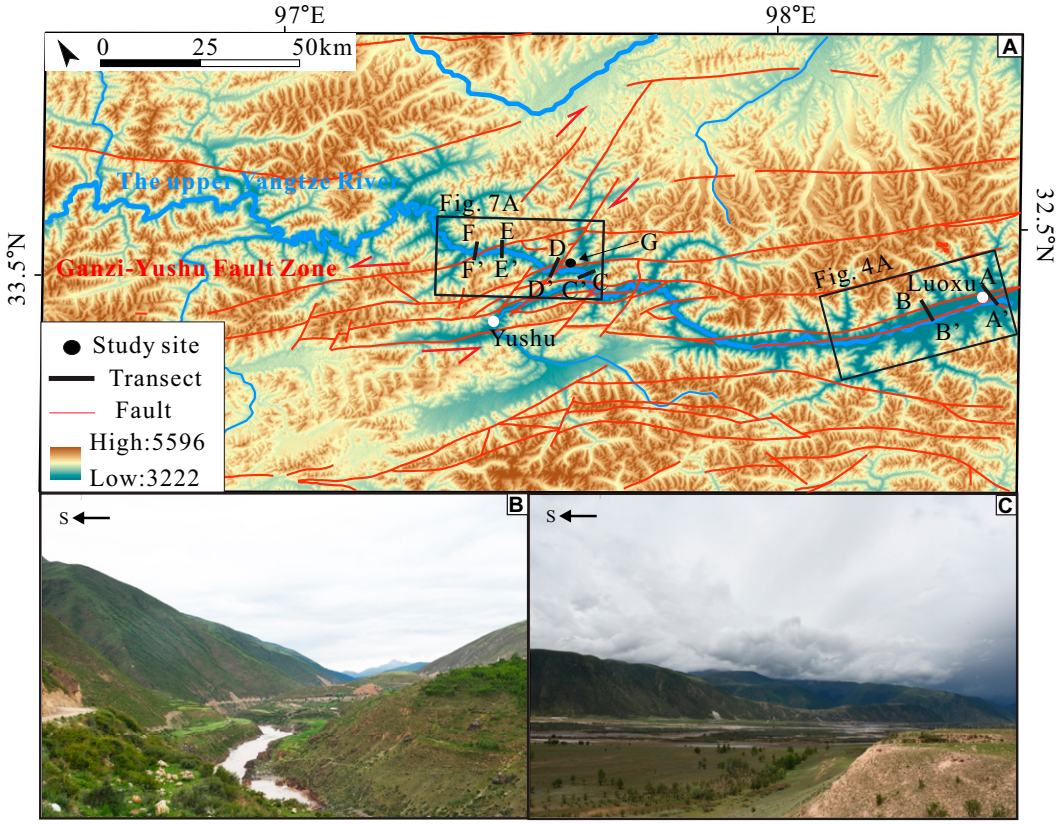

Figure 2. (A) Topographic map of the study area in the headwaters of the Yangtze River, eastern Tibetan Plateau, China. Depicted faults are from the China Geological Archives (1:500,000, http://www.ngac.org.cn/Map/List). The rectangles illustrate the areas with fluvial terraces in the Tongtian gorge and Luoxu basin. AA′, BB′, CC′, DD′, EE′, FF′ are seven studied transects in the upper Yangtze River catchment, G point is a site with typical interbedded fluvial, debris, and colluvium deposits. (B) The landscape of the gorge with deep incision and slopes in bare bedrock in the Yushu area. (C) Basin landscape with wide valley and slope with thick soil in the Luoxu area.

River into small blocks of local extent that have subsided and/or uplifted relative to each other. Fluvial aggradation in the subsided blocks contrasts with incision and formation of gorges in the uplifted blocks (Figs. 2B and 2C).

The study area in the headwaters of the Yangtze River is situated in the Alpine climate zone with strong winds and low temperature. The average annual temperature is below 0 °C. Currently, a mild and humid climate dominates the lower valley at the eastern edge of the Luoxu basin, eastern Tibetan Plateau, China (Fig. 2). The rainfall generally decreases from southeast to northwest, but increases significantly in the transitional area from the Luoxu basin to the Tongtian gorge because of the topographic effects (Fig. 3A).

The average elevation of the study area is ~4500 m. The northeastern part is flat with some wide glacial valleys, which contrast with the high relief deep valleys and inter-montane basins which are due to intensive fluvial incision and the fault activities in the southwest (Fig. 2). The headwaters of the Yangtze River flow over a distance of 350 km in the study area, and present steep channels in a detachment-limited condition (Rhoads, 2020) in the uplifted region (Yushu) (Fig. 2B) and graded channels in a transport-limited condition (Rhoads, 2020) in the subsided region (Luoxu) (Fig. 2C). Because of the heterogeneous tectonic background, this area is dominated by a deep-canyon (e.g., Tongtian gorge) in the uplifted region and a wide valley in the relatively subsided basins (e.g., Luoxu basin) (Fig. 3B) (Zhou et al., 2014). Two knickpoints are present along the Yangtze River in this region (Fig. 3B).

METHODS

Field Studies

River terraces have been well developed along the river valley in the headwaters of the Yangtze River. Here, the terrace sequence was determined based on height of terrace surfaces above present floodplain (apf) and the spatially continuous extension of terrace outcrops. We mapped the sequence of fluvial terraces by the combination of field investigations and remote-sensing images.

Six geomorphic transects were selected as representative of the suite of fluvial terraces. Two of those transects, AA′ and BB′ are located in the Luoxu basin (N32.55°–32.44°, E97.69°–98.03°), a tectonically relatively subsided (less uplifted) block (Fig. 2), while other transects CC′ (at the site of Shaijingtai, N33.00°, E97.25°), DD′ (at the site of Moluo, N33.00°, E97.21°), EE′ (at the site of Zhongda, E97.11°, N33.14°), and FF′ (at the site of Baliria, E97.06°, N33.17°) are distributed along the Tongtian gorge in a relatively uplifted block (Fig. 2). The site G (Zhimenda, N33.00°, E97.24°) shows a typical sequence of inter-bedded fluvial sediments and mass-flow sediments such as debris flows (see discussion) (Fig. 2). The terrace elevations were accurately measured using GPS with a maximum error of 5 m. Sedimentary structures were described according to the facies codes of Miall (1996).

OSL Dating

OSL samples were taken from different terraces (Table 1) by hammering a steel tube 25 cm long with a diameter of 5 cm into the sand layers of fresh sections. Pure quartz was extracted from the middle part of the tubes using common methods (30% H_2O_2, 10% HCl, wet sieving, 40% HF).

All the luminescence analyses were carried out on an automated Risø reader equipped with blue (470 nm; ~80 mW/cm^2) Light emitting diodes and infrared (IR) laser diode (870 nm, ~135 mW/cm^2). Quartz OSL signals were collected through a 7.5 mm Schott U-340 ultraviolet glass filter (emission 330 ± 35 nm). The quartz equivalent doses (De) were measured using a standard single-aliquot regenerative dose

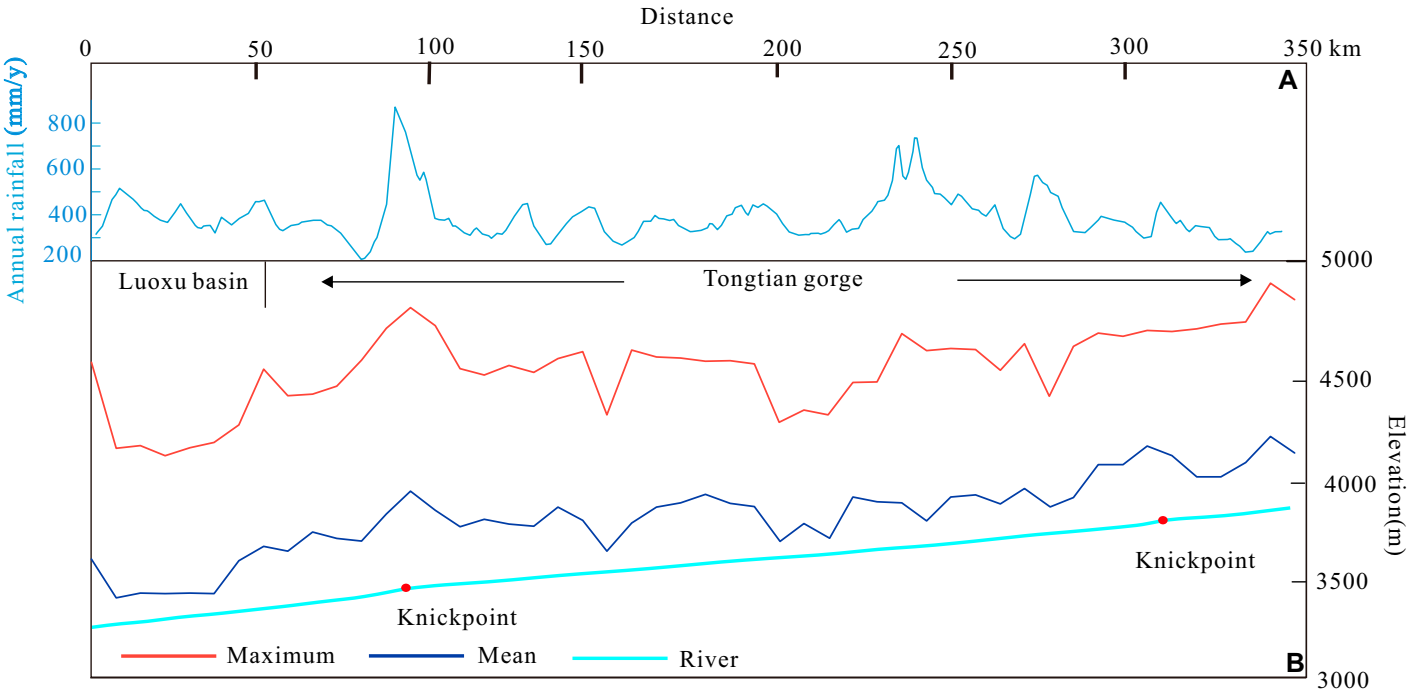

Figure 3. (A) The annual rainfall along the valley of the upper Yangtze River, eastern Tibetan Plateau, China. (B) Maximum (red) and mean (blue) elevation of a swath profile (5 km × 350 km) along the upper Yangtze River and the longitudinal profile of the Yangtze River (fluorescent-blue). Two knickpoints are present in this region.

protocol (Murray and Wintle, 2000, 2003). Preheating of the natural and regenerative doses was initiated for 10 s at 240 °C, and the response to the test dose was measured after a cut-heat of 200 °C. Optical stimulation with the blue diodes was conducted for 40 s at 125 °C. The initial 0.16 s of the decay curve was used in the calculations, minus a background evaluated from the following 0.16–0.32 s. After measurements of the response to the test dose, a high-temperature bleaching was performed by stimulating with the blue diodes for 40 s at 280 °C (Murray and Wintle, 2003). For each aliquot, the dose response was obtained from measurements of the response to four regenerative doses. This was followed by three additional measurements to obtain estimates of recuperation and recycling (Murray and Wintle, 2000) and purity test (OSL IR depletion ratio; Duller, 2003). All the above laboratory measurements were carried out at the Luminescence Dating Laboratory of the geomorphic process team, of the School of Geography and Ocean Science, Nanjing University, Nanjing, China.

The sediments at both ends of the tubes were used for water content and radioactive element analysis. The material (~20 g) was first dried

TABLE 1. SUMMARY OF SAMPLE CODE; U, Th, AND K CONCENTRATIONS, ESTAMATES OF PAST WATER CONTENT (W.C.), DOSE RATES, EQUIVALENT DOSES (De), OVERDISPERSION (OD), AND AGE FOR FLUVIAL SEDIMENTS, EASTERN TIBETAN PLATEAU, CHINA

Field code	Grain size (μm)	Depth (m)	U (ppm)	Th (ppm)	K (%)	W.C. (%)	Dose rate (Gy/ka)	De (Gy)	OD (%)	Age (ka)
LX-OSL-110	63–90	1.1	1.43 ± 0.07	7.44 ± 0.37	1.26 ± 0.06	14 ± 7	2.32 ± 0.35	6.6 ± 0.6	28 ± 7	2.8 ± 0.3
LX-OSL-210	63–90	2.1	1.15 ± 0.06	5.43 ± 0.27	1.19 ± 0.06	16 ± 8	2.06 ± 0.3	10.5 ± 0.7	19 ± 4	5.1 ± 0.4
LX-B-OSL-100	63–90	1	2.31 ± 0.12	10.79 ± 0.54	1.67 ± 0.08	26 ± 13	2.79 ± 0.39	41.0 ± 1.5	9 ± 3	14.7 ± 1.2
LX-B-OSL-150	63–90	1.5	1.63 ± 0.08	7.02 ± 0.35	1.19 ± 0.06	15 ± 8	2.26 ± 0.34	34.6 ± 1.7	12 ± 4	15.3 ± 1.1
LX-C-OSL-60	63–90	0.6	2.26 ± 0.11	11.16 ± 0.56	1.56 ± 0.08	17 ± 8	2.93 ± 0.45	6.4 ± 0.2	4 ± 2	2.2 ± 0.1
LX-C-OSL-160	63–90	1.6	2.43 ± 0.12	9.72 ± 0.49	1.44 ± 0.07	32 ± 16	2.46 ± 0.32	46.9 ± 2.0	10 ± 4	19.0 ± 1.8
LX-D-OSL200	63–90	2	2.00 ± 0.10	8.69 ± 0.43	1.36 ± 0.07	18 ± 9	2.54 ± 0.38	40.2 ± 1.5	8 ± 3	15.8 ± 1.1
LX-D-OSL450	63–90	4.5	1.36 ± 0.07	6.57 ± 0.33	1.27 ± 0.06	13 ± 7	2.25 ± 0.34	35.6 ± 2.1	9 ± 6	15.8 ± 1.2
LX-E-OSL-100	63–90	1	2.06 ± 0.10	11.38 ± 0.57	1.74 ± 0.09	21 ± 10	2.95 ± 0.44	6.6 ± 0.2	6 ± 2	2.2 ± 0.2
LX-E-OSL-220	63–90	2.2	2.11 ± 0.11	11.18 ± 0.56	1.74 ± 0.09	34 ± 17	2.66 ± 0.35	48.0 ± 1.5	7 ± 3	18.0 ± 1.7
LX-E-OSL-650	63–150	6.5	1.29 ± 0.06	6.71 ± 0.34	1.38 ± 0.07	16 ± 8	2.30 ± 0.34	54.2 ± 3.0	17 ± 6	23.6 ± 1.7
SJT-OSL-1	63–90	4	1.59 ± 0.08	8.16 ± 0.41	1.49 ± 0.07	35 ± 17	2.26 ± 0.68	42.3 ± 1.7	7 ± 3	14.9 ± 1.5
SJT-OSL-2	63–90	5.5	1.41 ± 0.07	7.10 ± 0.35	1.28 ± 0.06	13 ± 7	2.36 ± 0.36	33.5 ± 1.3	7 ± 5	14.2 ± 0.9
SJT-OSL-3	90–150	12	1.43 ± 0.07	6.79 ± 0.34	1.58 ± 0.03	19 ± 9	2.05 ± 0.14	42.1 ± 1.5	19 ± 7	20.5 ± 1.5
ZD-OSL-1	63–90	5	2.18 ± 0.11	8.74 ± 0.44	1.44 ± 0.07	17 ± 8	2.69 ± 0.40	39.5 ± 1.4	8 ± 4	14.7 ± 1.0
ZD-OSL-2	63–90	37	1.94 ± 0.10	10.46 ± 0.52	1.54 ± 0.07	12 ± 6	2.94 ± 0.47	55.9 ± 1.7	3 ± 6	19.0 ± 1.1
BLRA-OSL-1	63–90	3	1.12 ± 0.06	5.52 ± 0.28	1.00 ± 0.05	15 ± 8	1.93 ± 0.27	11.3 ± 0.6	16 ± 4	5.8 ± 0.4
BLRA-OSL-2	63–90	5	1.42 ± 0.07	6.55 ± 0.33	1.17 ± 0.06	16 ± 8	2.20 ± 0.32	28.8 ± 1.9	16 ± 5	13.1 ± 1.1
BLRA-OSL-3	63–90	2	1.33 ± 0.07	6.72 ± 0.34	1.21 ± 0.06	11 ± 5	2.32 ± 0.36	21.5 ± 1.0	12 ± 3	9.3 ± 0.6
ML-OSL-2	90–150	6.5	1.19 ± 0.06	7.64 ± 0.38	1.37 ± 0.07	14 ± 7	2.39 ± 0.36	570.3 ± 64.9	23 ± 10	238.2 ± 30.0
ZMD-A-OSL-1	63–90	1.5	2.27 ± 0.11	11.11 ± 0.56	2.21 ± 0.11	20 ± 10	3.41 ± 0.53	83.6	29 ± 10	24.5 ± 5.6
ZMD-A-OSL-2	90–150	11.5	1.53 ± 0.08	7.78 ± 0.39	1.61 ± 0.08	23 ± 11	2.48 ± 0.35	49.8 ± 2.2	9 ± 4	20.1 ± 1.7
ZMD-A-OSL-3	63–90	12	1.32 ± 0.07	6.95 ± 0.35	1.38 ± 0.07	16 ± 8	2.35 ± 0.35	13.5 ± 0.2	4 ± 2	5.7 ± 0.3
ZMD-1	63–90	30	2.03 ± 0.10	9.92 ± 0.50	1.44 ± 0.03	0.6 ± 0.3	2.67 ± 0.58	51.5 ± 1.9	6 ± 3	19.3 ± 0.8
ZMD-2	63–90	35	2.13 ± 0.11	10.88 ± 0.54	1.59 ± 0.03	1.2 ± 0.6	2.87 ± 0.61	54.5 ± 1.6	4 ± 4	18.9 ± 0.6

and then ground to powder to determine concentrations of U, Th, and K using inductively coupled plasma–mass spectrometry and inductively coupled plasma–optical emission spectrometry at the Geochemistry Laboratory of the School of Earth Sciences and Engineering, Nanjing University. Because the water content will have varied during the long-term burial period, we assumed 50% of the saturated water content as the average value during historical time with an uncertainty of 50% for this value to allow for possible fluctuations. Based on applying conversion factors from Guérin (Guérin et al., 2011) and beta attenuation factors from Mejdahl (Mejdahl, 1979), the external beta and gamma dose rates were calculated using the radionuclide concentration.

RESULTS AND INTERPRETATION

Terraces in the Relatively Subsided (Less Uplifted) Luoxu Basin

In the Luoxu basin, a relatively subsided region, we found seven terraces with characters of wide and flat landforms (Fig. 4).

The AA′ Section

Three terraces correlate with T7, T4b, and T1 (see terrace correlation below) in the transect AA′ (Figs. 2, 4, and 5A). Gravels in all terrace deposits consist of quartzite, sandstone, granite, conglomerate, and diabase. The sediment of T7 (62 m apf) was divided into three units from the bottom to the top (Figs. 5A and 6A). The basal unit (36 m thick) is mainly composed of poorly sorted gravels and deposited as planar cross-bedded (Gp facies) and disorganized, clast-supported beds (Gcm facies) (Figs. 5A and 6A). The base of the gravels is not exposed. The gravels are mainly rounded to sub-rounded, 10–20 cm in diameter. The middle unit (1.5 m thick) is fine sand with a massive structure (Sm facies). The top unit (0.5 m thick) is silt with small pebbles, showing a massive structure (Fm facies) (Fig. 6A).

T4b is at 28 m apf in transect AA′ (Fig. 5A). We divide the sediment into two units from the bottom to the top (Figs. 4, 5A, and 6B). The basal unit (1 m thick) consists of imbricated gravels with planar cross bedding (Gp facies) and occurs in organized, clast-supported beds

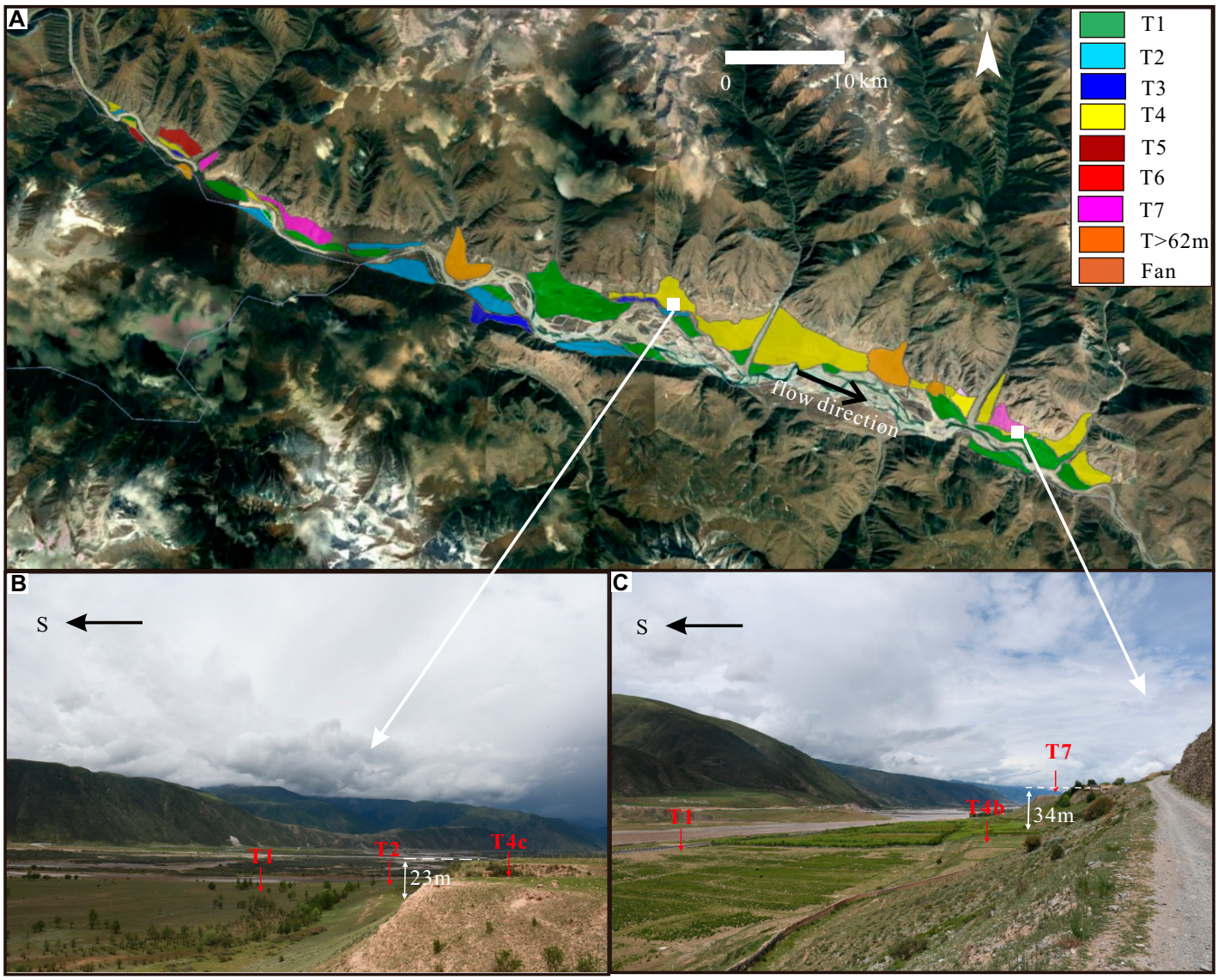

Figure 4. (A) Terrace distribution in the Luoxu basin, eastern Tibetan Plateau, China. (B and C) are the photos in the transect BB′ and AA′, respectively.

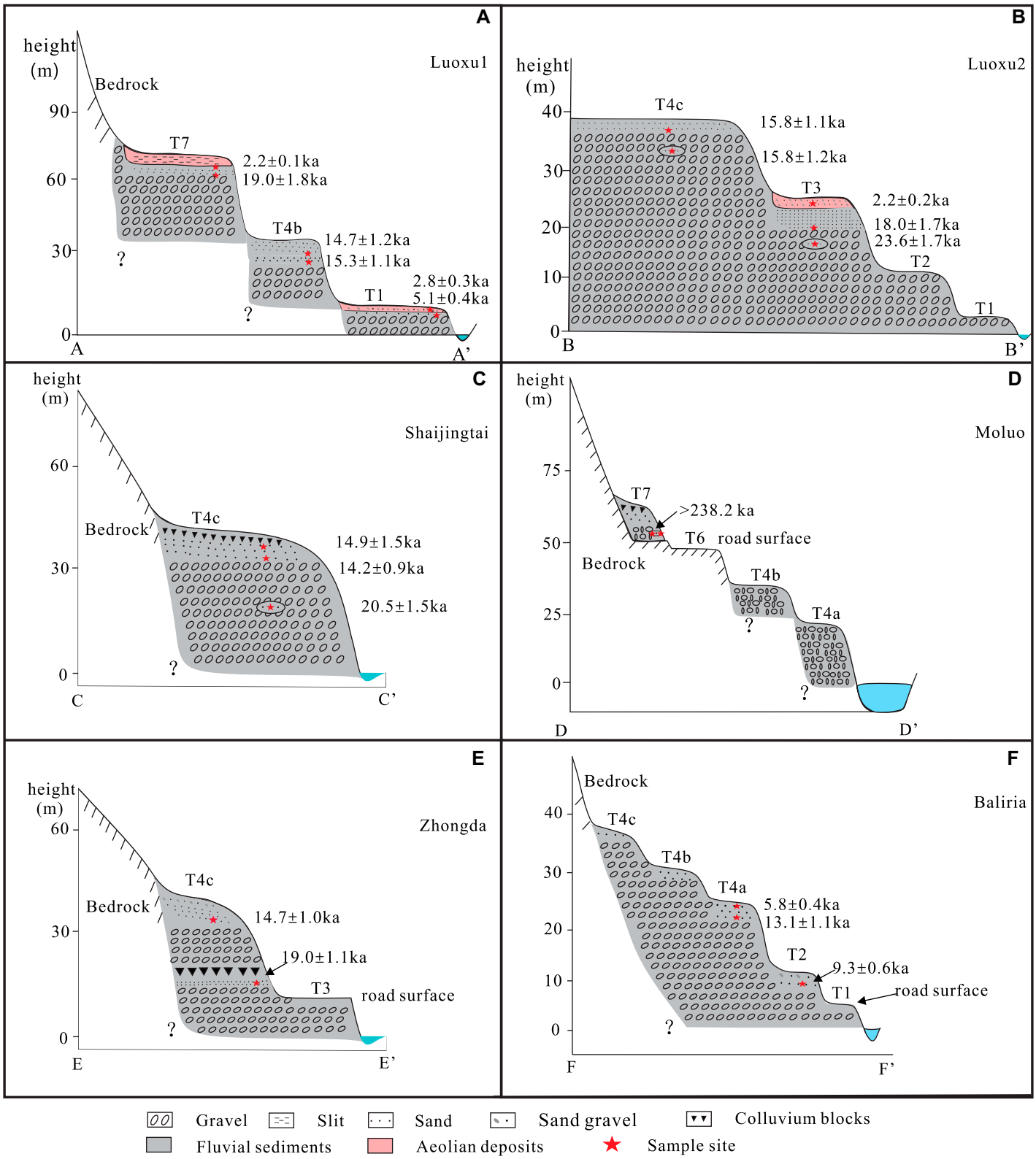

Figure 5. Schematic cross sections and ages along the studied geomorphic transects (see their locations in Fig. 2). (A–F) are the terraces at transects AA′, BB′, CC′, DD′, EE′, FF′, respectively.

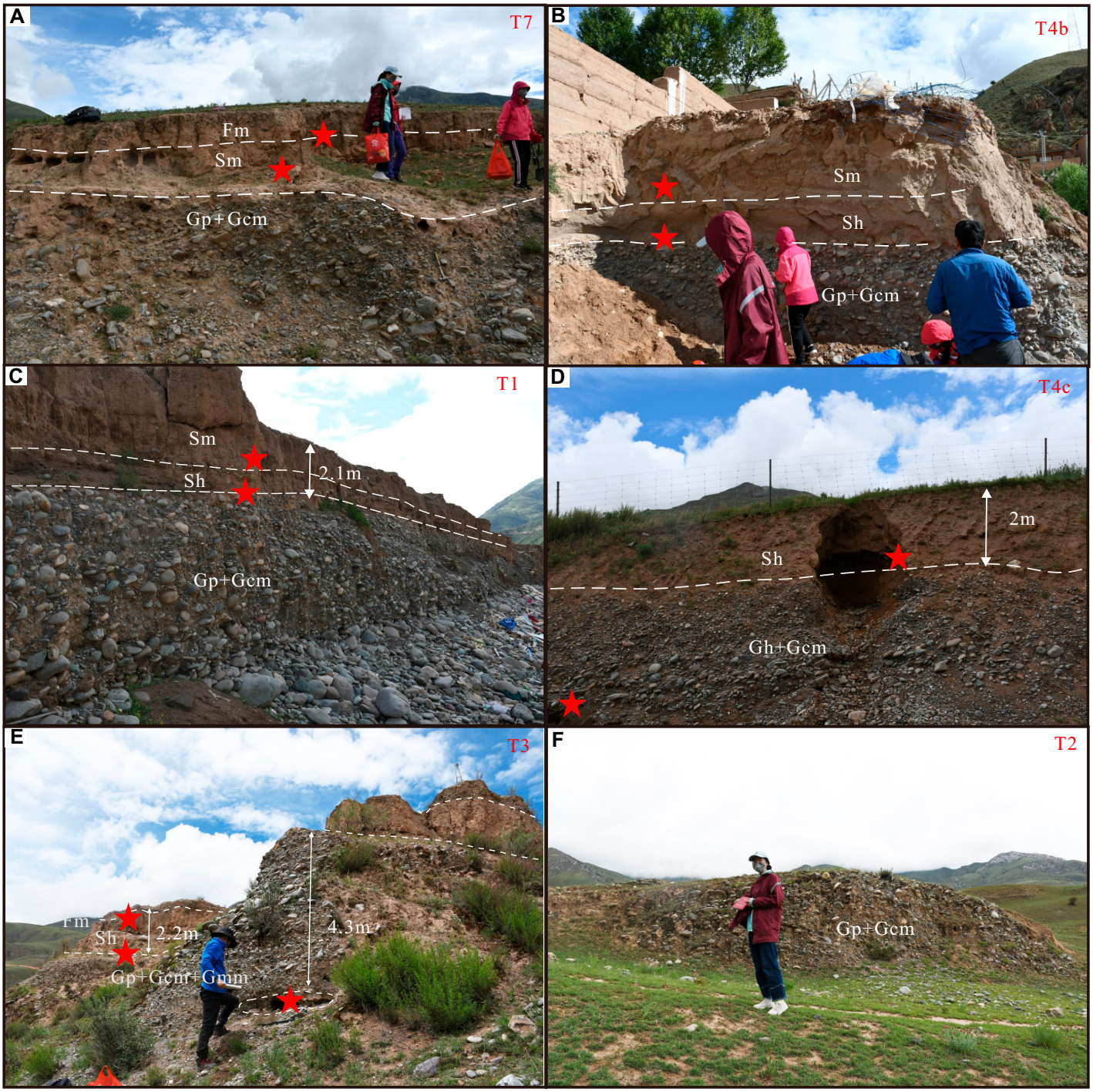

Figure 6. The sedimentary structure of sediments at terraces (A) T7, (B) T4b, (C) T1, (D) T4c, (E) T3, and (F) T2 in the Luoxu basin, eastern Tibetan Plateau, China. The red star marks the location of optically stimulated luminescence samples. Fm—massive silt; Sm—massive sand; Sh—horizontal laminated sand; Gh—horizontal gravels; Gp—gravels with planar cross bedding; Gcm—clast supported gravels. The dashed line marks the boundary between different units.

(Gcm facies) (base not exposed) (Figs. 5A and 6B). The gravels are mainly rounded, 10–20 cm in diameter. The top unit (1.6 m thick) is sand with small pebbles. The lower part of that upper unit is coarse sand with horizontal lamination (Sh facies), and the topmost part is fine sand with a massive structure (Sm facies) (Fig. 6B).

The lowest terrace (T1) is at 5 m apf. We divide the sediments into three units (Figs. 4, 5A, and 6C). A 5 m thickness of imbricated gravels make up the bottom unit without exposed base and deposited as planar cross-bedded (Gp facies) and disorganized, clast-supported layers (Gcm facies). The grain sizes of the gravels decrease upward from 10–30 cm to 5–8 cm in diameter. The middle unit (0.5 m thick) is coarse-grained sand with horizontal lamination (Sh facies). The

top unit (1.6 m thick) is reddish silt with a massive structure (Sm facies) (Fig. 6C).

All the sediments of T7, T4b, and T1 show channel deposition of rounded and imbricated gravels at the base, followed by overbank deposition (with laminated structure) and/or aeolian sedimentation (with massive structure). The disorganized and massive gravels in the Gcm facies indicate rapid deposition by high concentrated stream flow, while the planar cross-beds in facies Gp are interpreted as the foresets of transverse 2-D gravel bedforms (Miall, 1996). The sand in Sh facies suggests deposition by planar bed flows in channels, or sheet flood in upper-flow regime, while the massive structure (Sm and Fm facies) is due to rapid deposition of sand from the suspended load of waning flows in overbank or abandoned channels (Miall, 1996).

The BB′ Section

The four terraces in transect BB′ correlate with T4c, T3, T2, and T1 (see terrace correlation below) (Figs. 2, 4, and 5B). Gravel composition is similar in all terrace deposits, dominated by sandstone, granite, conglomerate, diabase, and quartzite. T4c at 34 m apf contains two units (Fig. 6D). The basal unit (4 m thick) is composed of imbricated gravels, deposited in horizontal beds (Gh facies) with some sand lenses, and organized in clast-supported beds (Gcm facies) (Fig. 6D). The base of this unit is not exposed. The gravels are rounded with upward decreasing size from 10–20 cm to 5 cm diameter. The top unit (2.5 m thick) is sand with some pebbles, showing horizontal lamination (Sh facies).

The T3 surface is underlain by a lower 18-m-thick gravel and an upper 2.5-m-thick bed of fine sand with small pebbles (Figs. 5B and 6E). The structure of the gravel unit is planar-cross bedded (Gp facies) with some sand lenses, and occurs in disorganized, clast-supported and, matrix-supported beds (Gcm and Gmm facies) (Fig. 6E). The base of this unit is not exposed. The gravels are rounded, 30–50 cm and 10–20 cm in diameter. The top unit (2.5 m thick) mainly consists of sand with some pebbles (Fig. 6E). The lower part of this unit shows horizontal lamination (Sh facies), while the upper part is a fine silt with massive structure (Fm facies) (Fig. 6E).

T2 and T1 extend at 13 m and 2 m apf along the river, respectively (Fig. 5B). All the units consist of imbricated gravel deposits with planar-cross bedding (Gp facies) and are organized in clast-supported beds (Gcm facies). The gravels are round, 20–30 cm in diameter. In contrast to the higher terraces, no fine-grained sediment covers the gravels of these terraces (Fig. 6F).

The gravels of the terraces in transect BB′ were deposited by channel traction flow as indicated by the rounded shape and the imbricated traction structures (e.g., Gp facies). The sedimentary structures of all outcrops are similar to those in transect AA′, indicating similar sedimentary processes and environments.

Terraces from the Gorges in Relatively Uplifted Segments

In contrast to terraces in the Luoxu basin, seven terraces in the uplifted Tongtian gorge are steep, narrow, and discontinuous (Fig. 7).

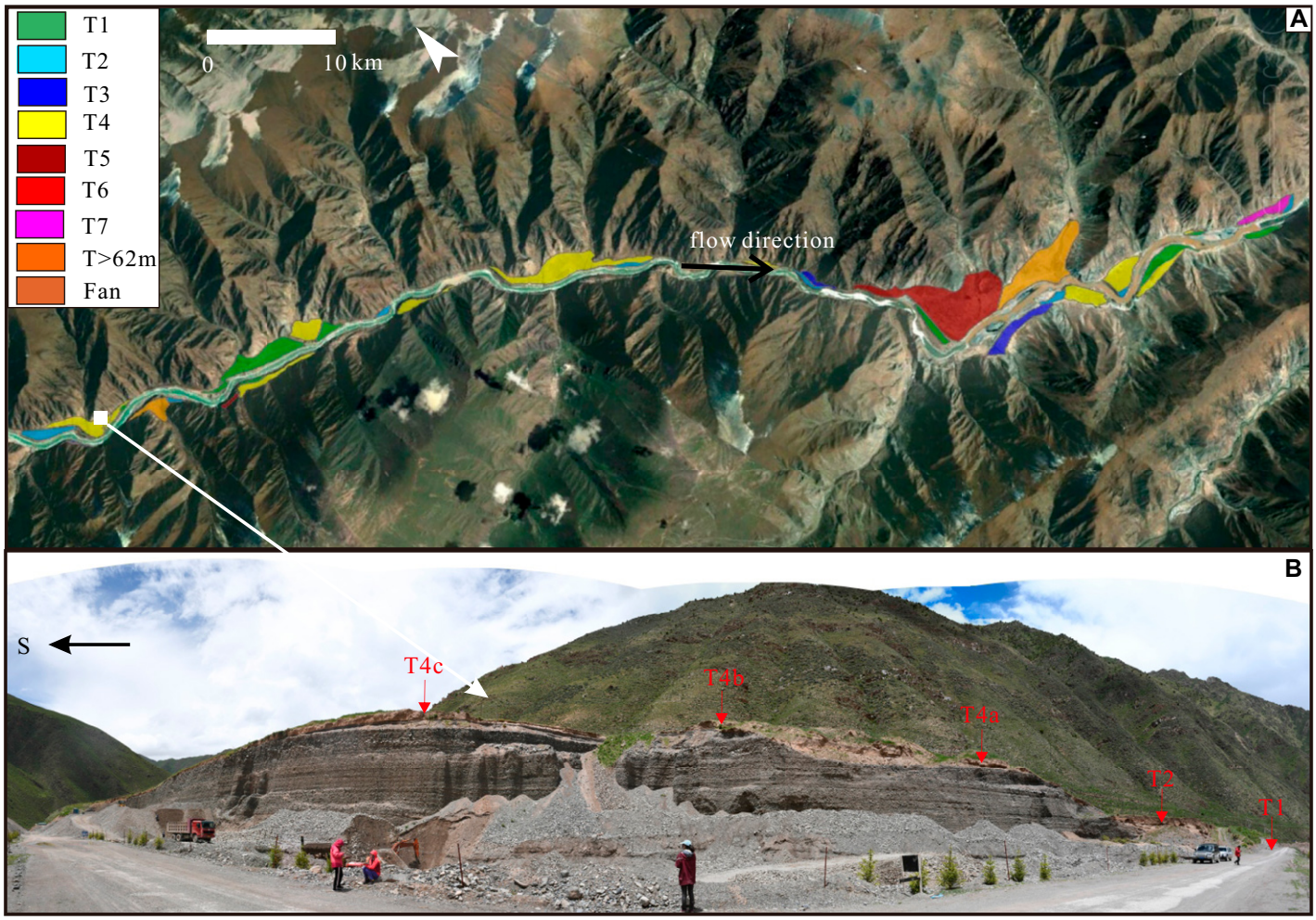

Figure 7. (A) Terrace distribution in the Tongtian gorge, eastern Tibetan Plateau, China. (B) The photos of cut-in-fill terraces in the transect FF′.

The CC′ Section

One terrace, T4c (see terrace correlation below), is identified in this section (Figs. 2, 5C, and 8A) at Shaijingtai (SJT; N33.00°, E97.25°) at 34 m apf. It contains gravels, sand, and angular blocks from the bottom to the top (Fig. 5C). We divided the sequence into three units according to the particle size and structural characteristics of the sediments (Fig. 8A). The lowest unit is dominated by imbricated gravels, deposited as planar-cross (Gp facies) and clast-supported beds (Gcm facies) (Fig. 8A). The base of this unit is not exposed. The gravels are sub-rounded to rounded, 20–40 cm in diameter, and consist of diabase, sandstone, conglomerate, and granite.

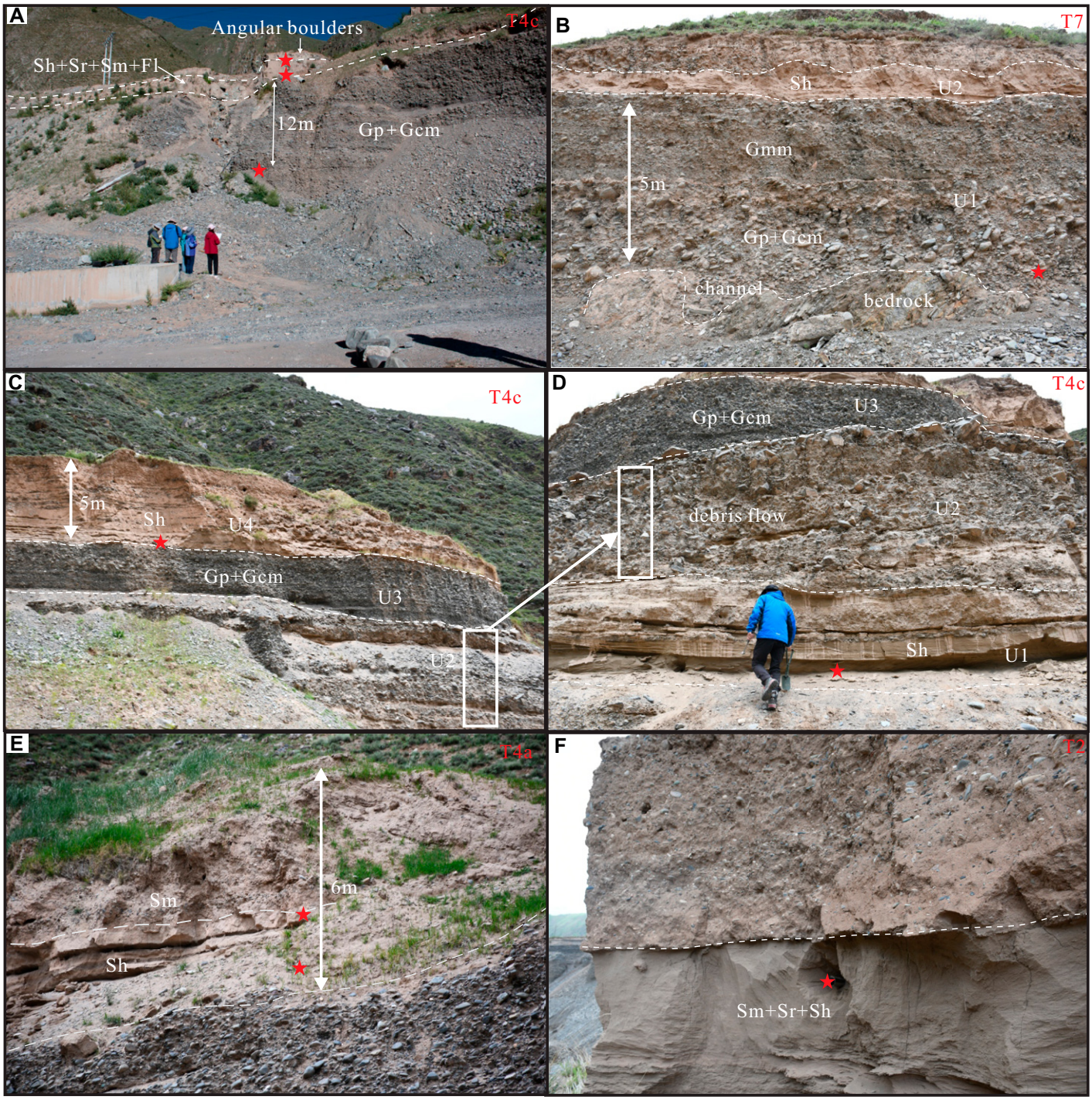

Figure 8. Terraces and sediments in the Tongtian gorge, eastern Tibetan Plateau, China. (A) The sedimentary profile of T4c in transect CC′. (B) The sedimentary profile of T7 in transect DD′. (C and D) are the sedimentary profiles of T4c in transect EE′. (E and F) are the sedimentary profile of T4a and T2 in transect FF′. The red stars mark the location of optically stimulated luminescence samples. Sm—massive sand; Sh—horizontal laminated sand; Gp—planar cross bedding gravel; Gcm—clast-supported gravel beds; Gmm—matrix-supported gravel beds. The dashed line marks the boundary between units.

The middle unit (2.3 m thick) is composed of sand in its lower part and silty sand in its upper part. The sand deposit shows mainly horizontal lamination (Sh facies) with occasional small ripples (Sr facies) and massive structure (Sm facies) (Fig. 8A). The silty sand shows also small ripple structures (Fl facies). The top unit is composed of chaotically structured, angular boulders (gray-green breccia, 10–15 cm in diameter) (Fig. 8A).

The structure of sediments in transect CC′ shows a fluvial origin, covered with some sediments of mass-flow origin. Again, the poorly sorted, sub-rounded to rounded gravels in the Gcm facies indicate rapid aggradation as a channel lag deposit, while the planar-cross beds (Gp facies) represent the foresets of low bars and dunes. The sand layers with horizontal lamination, cross bedding, and massive structure show an upward decrease from coarse sand to fine sand, meaning a decline of transport energy. The small ripple (Fl facies) in silt indicates abandoned channel fills, while the chaotically angular gravels with oversized blocks are interpreted as debris flow sediments or landslide sediments.

The DD′ Section

Four terraces here correlate with T7, T6, T4b, and T4a (see terrace correlation below) (Figs. 2 and 5D). T7, at 55 m apf, is poorly preserved along the northern bank of the Yangtze River at the site of Moluo (ML) (N33.00°, E97.21°) (Figs. 5D and 8B). The sediment sequence in that terrace comprises three units (Fig. 8B). The lowest unit 1 (5 m thick) is composed of imbricated gravels with inter-fingering sand lenses. Toward the base the gravels are rounded to sub-rounded, 10–50 cm in diameter, deposited as planar-cross beds (Gp facies), and clast-supported (Gcm facies) (Fig. 8B). Toward the top of unit 1 the gravels are angular to sub-angular, 5–15 cm in diameter, and matrix-supported (Gmm facies) (Fig. 8B). All the gravels are composed of sandstone, diabase, granodiorite, quartzite, conglomerate, and limestone. Unit 2 (3 m thick) in the middle part of the section is composed of sand layers with horizontally laminated structure (Sh facies). Some cm-scale angular pebbles are present inside the sand layer. The top unit 3 consists of disorganized gray-green angular blocks, 40–50 cm in diameter.

T6 at 42–46 m apf shows multiple cycles of channels, debris, and colluvial sediments. The base of this sediment sequence is not exposed. T4b and T4a extend along the steep slope with poorly organized gravel structure (Fig. 5D). Because of the deep incision with a steep slope, it was impossible to sample the sections and to describe the sedimentary structure in detail.

The sedimentary structures of Gp, Gcm, and Sh facies with imbricated gravels, rounded and sub-rounded gravels in the layers of T7, show stream channel flow (Miall, 1996). In contrast, the disorganized angular gravel and matrix-supported gravels layers in unit 3 and the upper part of unit 1 suggest debris flow sediments or sediments resulting from mass wasting process from the hillslope (e.g., Hewitt et al., 2008).

The EE′ Section

The two terraces in this section correlate with T4c and T3 in Zhongda (ZD; E97.11°, N33.14°) (Figs. 2 and 5E) (see terrace correlation below). The gravels are composed of sandstone, diabase, granodiorite, quartzite, conglomerate, and limestone. T4c and T3 occur at 34 m and 18 m apf, respectively (Fig. 5E). The base of T4c is a set of gravel layers with sand (Fig. 8C). The sedimentary sequence of this terrace is subdivided into four units (Figs. 5E, 8C, and 8D). The unit 1 (3 m thick) is a horizontally laminated sand layer that contains several thin layers of angular small pebbles (Fig. 8D). The overlying unit 2 (5 m thick) is composed of disorganized blocks (Figs. 8C and D) which are angular with upward increasing diameter (cm- to m-scale; Fig. 8C). A 4-m-thick gravel layer (unit 3) covers unit 2. It shows an imbricate structure, with planar-cross bedding and clast-supported beds (Gp and Gcm facies) (Figs. 8C and 8D). The gravels are sub-angular to sub-rounded, 20–30 cm in diameter. Unit 4 (5 m thick) is composed of sand with some cm-scale pebbles in the upper part, showing a horizontally laminated structure (Sh facies) (Fig. 8C).

T3 is composed of gravels with unexposed base, on which a road was constructed without outcrop. The structure of disorganized gravels with appearance of oversized blocks (unit 1 and the bottom of unit 2) in the T4c sediment sequence shows a debris flow origin (e.g., Li et al., 2018) (Figs. 8C and 8D). The multiple cycles of alternating fluvial sands with their typical characteristics and angular debris blocks within unit 1 of the T4c sediment sequence indicates a process of rapid succession of fluvial and mass-wasting origin. This may be an expression of the frequent interruption of the fluvial process (imbricated rounded gravels in Gp and Gcm facies of unit 3 in T4c sediments) by the supply of large angular debris from small tributaries and hillsides in the form of alluvial fans or debris slopes. Lateral erosion of the river in the gorge resulted in sporadic bedrock exposure along the hillslope.

The FF′ Section

In contrast to the sections described above, the gravels of transect of FF′ (see location in Figs. 2, 5F, and 7B) accumulated in a 33-m-thick layer. They were incised to form five terraces, T4c, T4b, T4a, T2, T1, at 33, 28, 22, 12, 5–6 m apf, in Baliria (BLRA; E97.06°, N33.17°), respectively (Figs. 5F and 7B). The composition of the gravels is similar to that in the previous transects. The gravels show imbrication, planar-cross bedding (Gp facies), and are clast-supported (Gcm facies), 20–30 cm in diameter (Fig. 7B). The base of the sediment sequence is not exposed.

T4c and T4b are covered with sand, but the outcrop, a cliff, was not accessible for description of the sedimentary characteristics (Fig. 7B).

T4a has two sediment units covering the underlying gravel fillings. The lower unit1 (4 m thick) is composed of sand with horizontally laminated beds (Sh facies) (Figs. 7B and 8E). The upper unit 2 (2 m thick) is a massive sand bed (Sm facies) with pebbles (Figs. 7B and 8E).

The sediment of T2 shows two units covering the underlying gravels (Fig. 7B). The lower unit 1 (1.5 m thick) is a sand layer with small ripple cross-lamination (Sr facies) in the lower part and horizontal laminated structure (Sh facies) in the upper part (Fig. 8F). The upper unit 2 (2 m thick) is a massive sand (Sm facies) layer with cm-scale pebbles (Fig. 8F). T1 coincides with the road surface without outcrop.

The gravels and sands in these cut-in-fill terraces show thick fluvial sediments. The lower gravels with Gcm and Gp facies and the upper cross-laminated, horizontally laminated, and massive sands (Sr, Sh, Sm facies) point to variable energy.

Correlation of the Terraces

Seven terraces were mapped along the river (labeled as T1 to T7 from young to old) (Figs. 5 and 9; Table 2). They are correlated on the base of elevation above the floodplain and age of deposits. In the Luoxu basin, they are typified by the shape of the wide valley and the low gradient of the riverbed (Figs. 4B and 4C) and show similar sedimentary properties: fluvial gravels of various thickness are interbedded with sand lenses, silts, and ultimately capped by pebbly sand (Figs. 4–6). In contrast, the gorge area (i.e., Yushu area) is characterized by its narrow transverse profile and steep valley sides, while the boulders and breccia between fluvial gravels and sands in the gorge terraces illustrate a provenance from the hillside or small tributaries (Figs. 5, 7, and 8). Terraces in the gorge, for example at Baliria, are relatively narrow and spatially discontinuous (Fig. 7), but they are wide and flat in the Luoxu basin (Fig. 4).

A Typical Sequence of Alternating Fluvial and Mass Waste Sedimentation

The interbedded fluvial, debris, and colluvial deposits are widespread in the gorge; one

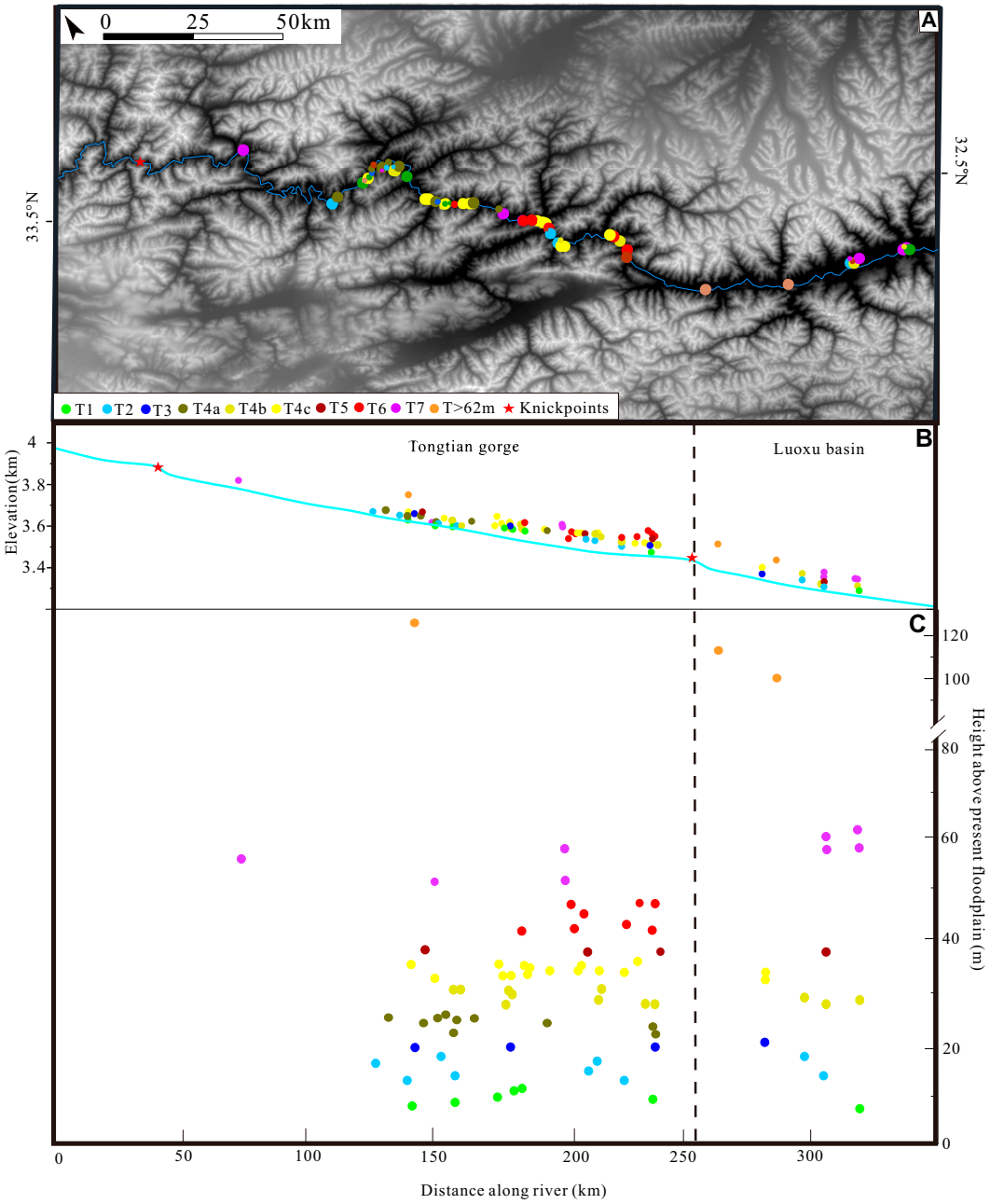

Figure 9. (A) Terrace distribution in the upper Yangtze River, eastern Tibetan Plateau, China. (B) The elevation of terraces and riverbed along the Yangtze River. The red stars indicate two knickpoints in the Yangtze River. (C) The terraces height above the present floodplain along the Yangtze River.

TABLE 2. THE ELEVATIONS ABOVE PRESENT FLOODPLAIN (apf), AGES, AND INCISION RATES (ELEVATION/AGE) AFTER TERRACE FORMATION IN THE LUOXU BASIN AND TONGTIAN GORGE, EASTERN TIBETAN PLATEAU, CHINA

Terrace sequence	Luoxu basin			Tongtian gorge		
	apf (m)	Terrace age (ka)	Incision rate (mm/yr)	apf (m)	Terrace age (ka)	Incision rate (mm/yr)
T7	62	19.0 ± 1.8	<3.3	55		
T6				42–46		
T5	38			38		
T4c	35	15.8 ± 1.1	2.2	34	17–13	2–2.6
T4b	28	15.3 ± 1.1	1.8			
T4a				22	13.1 ± 1.1	1.7
T3	18	<18.0 ± 1.7		18		
T2	13			11	9.3 ± 0.6	1.2
T1	5	5.1 ± 0.4	1.0	5		

typical sequence was described at the site of Zhimengda (ZMD, N33.00°, E97.24°) (site G in Fig. 2). The structure of the sedimentary section ZMD shows a sequence of alternating layers of rounded gravels, sands, and angular gravels and boulders, which may indicate alternating phases of fluvial and debris or colluvial deposition (Fig. 10). The top of the sediment sequence is ~53 m apf, which correlates with T7. The upper ~30 m sediments may be subdivided into eleven units (Fig. 10A). From bottom to top, unit 1 (5 m thick) is composed of disorganized

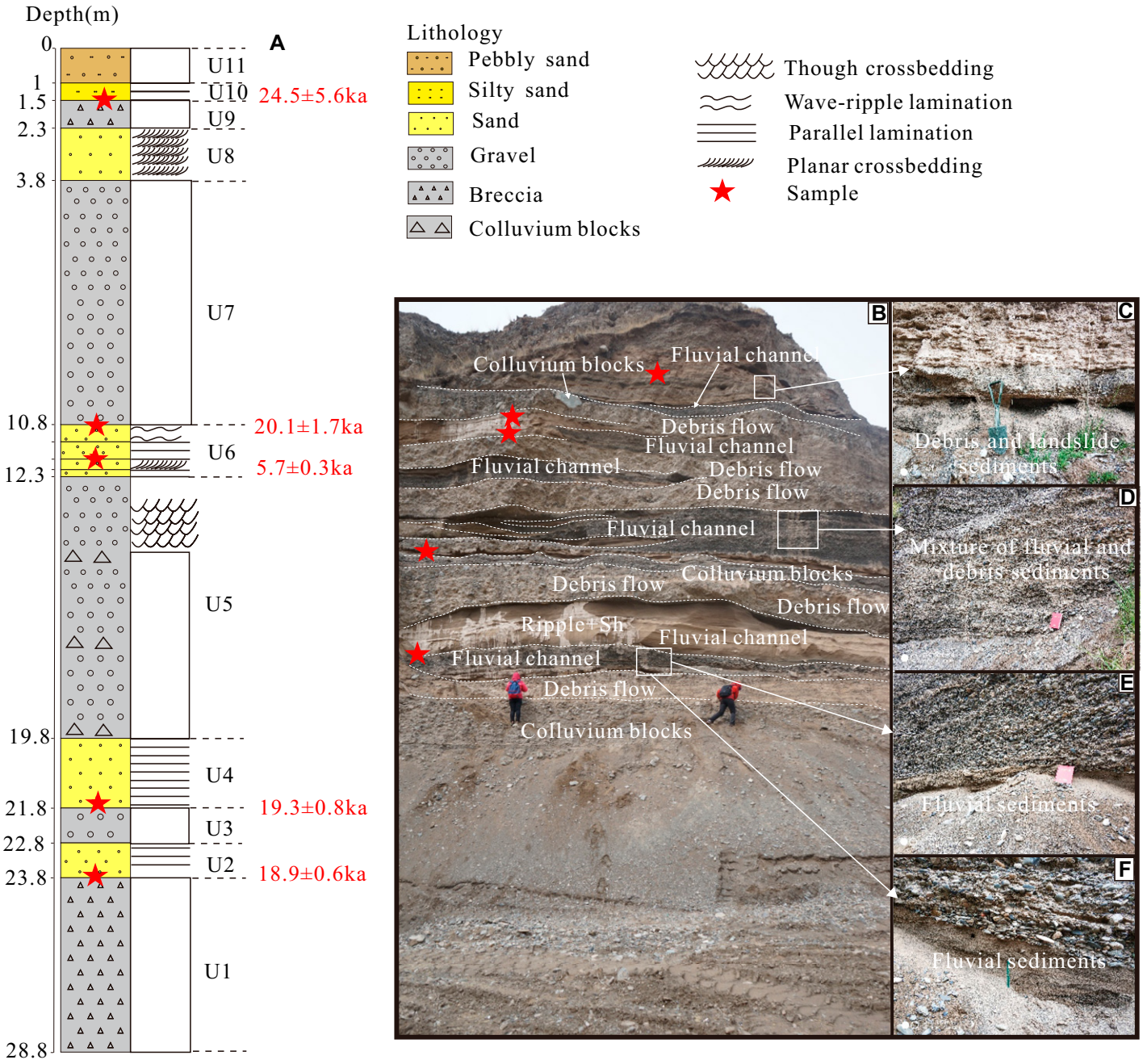

Figure 10. (A) Stratigraphic column, optically stimulated luminescence ages and location of samples at Zhimengda (ZMD), eastern Tibetan Plateau, China (units 1–11). (B) Typical sediments with alternating fluvial, debris, and colluvium beds at the ZMD site. White dashed line marks the boundary between units. (C and D) Mixture of fluvial and debris-flow sediments in Figure 10B. (E and F) are fluvial sediments in Figure 10B.

breccia, 5–10 cm in diameter. Unit 2 (1 m thick) is composed of sand with horizontally laminated structure (Sh facies). Unit 3 (1 m thick) contains imbricated gravels with planar cross-bedding and clast-supported beds (Gcm facies). The gravels are rounded, 10–20 cm in diameter, and consist of sandstone, diabase, quartz, conglomerate, and limestone. Unit 4 (2 m thick) is a horizontally laminated, fine-grained sand bed (Sh facies). Unit 5 (7.5 m thick) is composed of rounded gravels with planar cross bedding (Gp facies), trough cross-bedding (Gt facies), and clast-supported beds (Gcm facies), containing three layers of angular boulders (0.5–1 m in diameter). Unit 6 (1.5 m thick) is composed of sand with planar cross-bedding (Sp), horizontal lamination (Sh), and ripple cross-bedding (Sr) from bottom to top. Unit 7 (7 m thick) is composed of rounded gravels (5–10 cm in diameter) with planar cross-bedding (Gp facies) and gravel sheets with imbrication. The 1.5 m thick coarse sand layer of unit 8 is a deposit with planar cross-bedding (Sp facies) containing some angular pebbles (~1 cm in diameter). The overlying unit 9 (0.8 m thick) is a breccia (pebbles are 1–3 cm in diameter) with crude imbrication containing sand lenses with

planar cross-bedded structure (Sp facies). Unit 10 (0.5 m thick) is composed of horizontally laminated, silty sand (Fl facies) and sand (Sh facies). The topmost unit 11 (1 m thick) consists of angular gravels (2–6 cm in diameter) contained in a silt matrix.

The disorganized breccia in units 1 and 9 and the angular boulders in unit 5 are interpreted as debris flow or colluvial deposits. The rounded and sub-rounded gravels and sand with imbrication structures, planar or trough cross-bedding, horizontal lamination, and ripples in other units indicate a fluvial origin. The interbedded deposition of fluvial and debris and colluvial sediments points to a striking change in deposition conditions and provenance (e.g., Gao et al., 2018). They are the expression of the interplay between fluvial processes and mass-wasting events that characterizes the evolution in the gorge.

OSL Ages

The luminescence decay curves (Figs. 11A and C) show a rapid decrease, implying dominance of a fast component. The dose response curves are well-fitted with a single saturating exponential function (Figs. 11A and 11C). Their histograms of the equivalent dose illustrated by samples LX-E-OSL-220 and LX-E-OSL-100 show a normal distribution (Figs. 11B and 11D), indicating that the quartz is compatible with a well-bleached nature and the chronologic result is reliable. Table 1 summarizes the analytical data and OSL ages.

OSL dating results of fluvial, debris, and colluvium deposits in this region yield 25 ages ranging from 2.2 ka to 24.5 ka, except the sample ML-OSL-2 (Table 1). In the relatively subsided region (Luoxu basin), T7, T4c, T4b, T3, are dated at ca. 14–19 ka within the error margins, and T1 at ca. 5 ka (Table 1; Fig. 5). The bases of the gravel below terraces were not exposed, and gravels below different terraces show the same sedimentary structure and gravel composition. The age of 24 ka in sand lens at T3 at BB′ could indicate that the 62-m-thick fluvial sediments accumulated from >24 ka to 19 ka. The samples from the massive silty layers of top units with ages of 2.2 ka in T7, 2.8 ka in T1, and 2.2 ka in T3 reflect reworked aeolian sediments covering these terraces (Fig. 4).

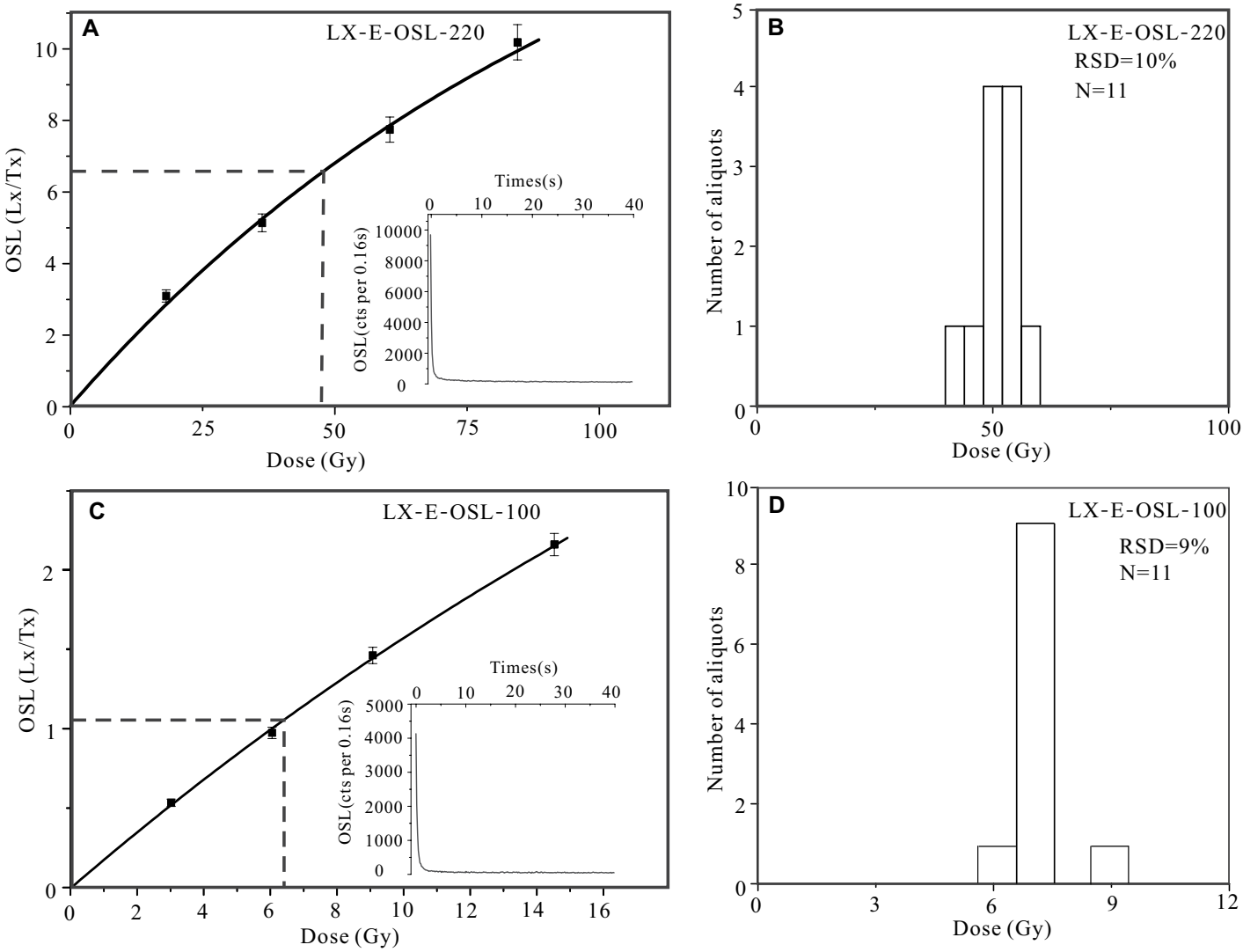

Figure 11. (A and C) are dose response curves for aliquots of samples LX-E-OSL-220 and LX-E-OSL-100 with inset figures showing the natural decay curves. (B and D) are histograms of equivalent dose distribution of samples LX-E-OSL-220 and LX-E-OSL-100. The samples LX-E-OSL-220 and LX-E-OSL-100 are taken from the site, Luoxu2 (N32.51°, E97.85°) (Fig. 5B). OSL—optically stimulated luminescence; RSD—relative standard deviation; cts—counts.

In the uplifted region (Tongtian gorge), the terraces T4c and T4a are dated at ca. 17–12 ka, and T2 at ca. 9 ka (Table 2; Fig. 4). The sand lens from the low part of the sediment sequence at SJT is dated at 20.5 ka, which means the thick gravels accumulated around >20.5 ka to 14.9 ka. The sand lens at site ZD is dated at 19 ka and demonstrates that debris-flow sediments (T4c in transect EE′) were deposited during the period 19.0–14.7 ka (Figs. 8C and 8D).The sand lens in the sediment sequence of ML is dated >238 ka, indicating former aggradation before 238 ka (Fig. 8B).

According to the definition of terrace ages (Vandenberghe, 2015), the age of a terrace is defined as the age of abandonment of the channels on its floodplain before incision, in other words lithologically corresponding with the boundary between gravel deposits and fine-grained floodplain deposits. It means that in this study the terrace age is just after the youngest age in the gravels (Table 2). The T3 at transect BB′ formed at <18 ka due to a sand layer which could be from valley filling was dated as 18 ka. The 20.5 ka and 24 ka in sand lens at SJT and BB′, and the similar sedimentary structure and gravel composition from these two sections reveal the valley in the headwaters of the Yangtze River has been filled with ~60-m-thick sediments before 19 ka. Subsequently, the river transformed from aggradation to generally continuous incision, episodically interrupted by phases of stability or lateral erosion. The latter interruptions initiated the formation of terraces at 62–38 m (T7–T5), 35–18 m (T4-T3), 13–11 m (T2), and 5 m (T1) above present floodplain, with ages of ca. 19 ka, ca. 17–13 ka, ca. 9 ka, and ca. 5 ka, respectively (Table 2).

As for the interbedded deposition of fluvial, debris, and colluvial sediments in ZMD, the OSL ages of 24.5 ka, 20.1 ka, 19.3 ka, and 18.1 ka in units 2, 4, 6, and 10, respectively, center at ca. 20 ka within the range of uncertainty of this kind of rapid deposition, except the age of 5.7 ka of unit 6 (Fig. 10). Thus, the interaction between fluvial, debris flow, and colluvial processes occurred at ca. 20 ka, during which the climate transformed from cold to warm. The age of 5.7 ka is to be considered an outlier and should be disregarded.

DISCUSSION

Response of Terrace Morphology to Tectonic Activities

Heterogeneous tectonic activities may result in relative uplift and subsidence, leading to different patterns of fluvial sedimentation and valley evolution in different parts of the drainage system (Whipple et al., 1999; Bridgland and Westaway, 2008; Vandenberghe et al., 2011; Wang et al., 2014; Duvall and Tucker, 2015). Indeed, the diverse tectonic activities in a catchment could cause considerable changes of local channel slope, which may lead to local changes in stream transport capacity and further fluvial responses in different tectonic blocks of the catchment. For example, the Huangshui River (NE Tibetan Plateau) incised and an erosion terrace developed in the uplifted areas (creating deep gorges), and meanwhile thick deposits formed an accumulation terrace in the subsiding areas (Wang et al., 2010, 2014; Vandenberghe et al., 2011).

In contrast to such a succession, the headwaters of the Yangtze River show similar sedimentary processes (a single thick valley filling followed by continuous incision) and terrace patterns (cut-in-fill terrace) both in the relatively uplifted (Tongtian gorge) and subsided (Luoxu basin) areas during the late Quaternary (Fig. 12). Compared to the Huangshui catchment, the headwaters of the Yangtze River occur at higher altitude and are characterized by stronger freeze-thaw processes, especially during the last ice age (Heyman et al., 2011; Ou et al., 2014), high relief

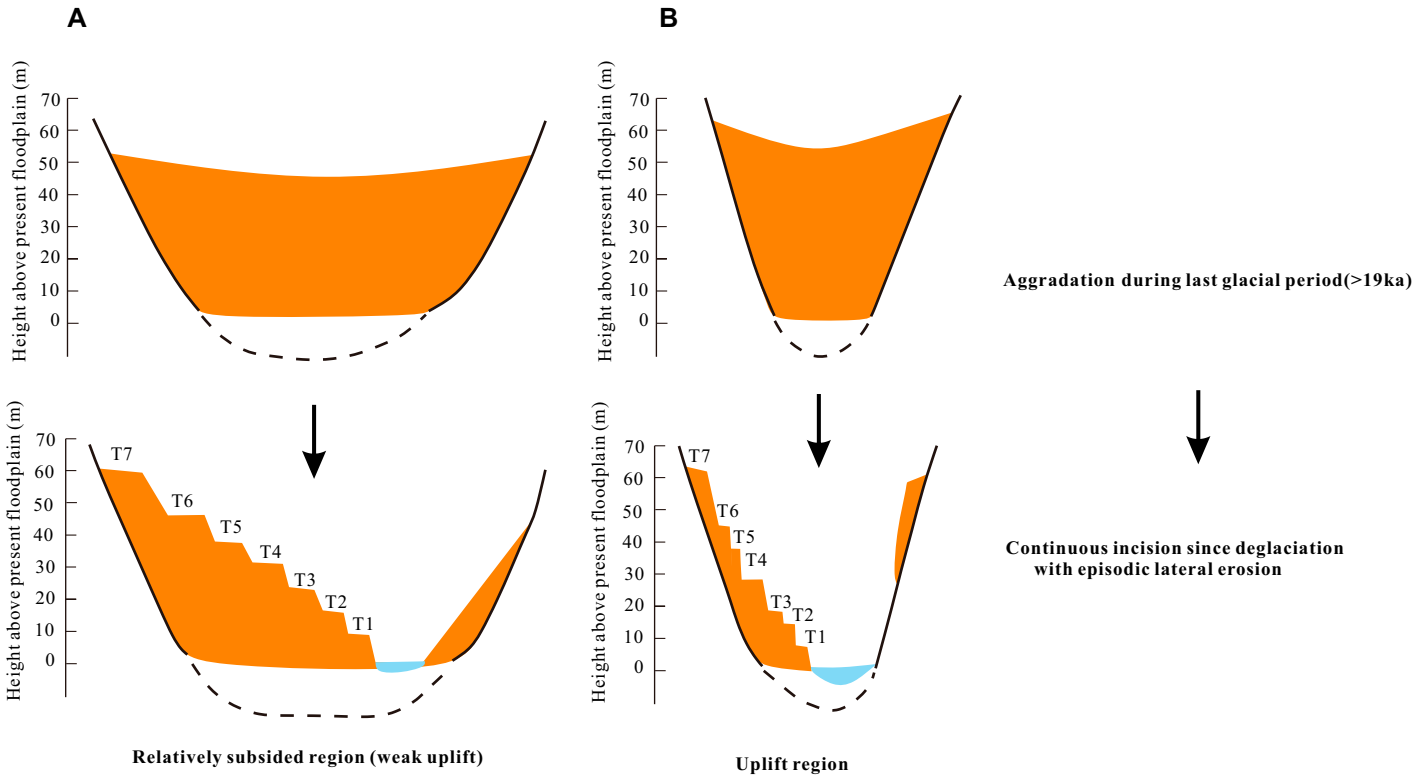

Figure 12. Conceptual model of different terrace morphology with accumulation mainly in the relatively subsided basins (Luoxu basin) (A) and formation of gorges in the relatively uplifted regions (Tongtian gorge) (B) in the headwaters of the Yangtze River during the late Quaternary, eastern Tibetan Plateau, China.

and frequent slope failures (Korup et al., 2010a). Large amounts of sediment supplied to the valleys in the headwaters of the Yangtze River during the last glacial maximum (LGM), may have resulted in the transition from detachment-limited to transport-limited conditions of the drainage system, and extremely thick valley aggradation at the maximum cold conditions. This exclusive aggradation may have restrained the effects of changing local valley slopes in the catchment caused by relative tectonic uplift and subsidence. In addition, similar incision rates in both uplifted and subsided areas reflect the negligible effects of tectonic movements on the terrace formation (Fig. 9; Table 2). Thus, if tectonic differentiation between the basins and uplifted regions may be excluded as a cause for the different kinds of terrace formation, we suggest that the immense amount of sediment input into the drainage system may be the primary steering factor for fluvial reaction (Fig. 12).

In spite of the similar terrace pattern and sedimentary processes in the subsided and uplifted areas, the spatial distribution and morphological outlook of the terraces are different in the individual tectonic blocks. The subsided area, the Luoxu basin, provides large storage space for lateral channel erosion and is characterized by wide and flat terraces in the center of the valley (Fig. 12A). In contrast, in the uplifted region, spaces are limited for lateral erosion, and narrow terraces extend stepwise along the valley sides. In the gorge, bedrock is sometimes exposed in spite of the cut-in-fill terrace style (Fig. 12B). This observation confirms that the uplift causes mainly downward erosion without terraces or with only narrow terraces along the river channel, while lateral erosion contributes to the formation of wide terraces in the case of subsidence (e.g., Wang et al., 2015; Bender et al., 2016, 2019).

Response of Terrace Formation to Climate Change

During the LGM, low temperature and humidity and weak monsoon activity (Figs. 13C and 13D) were favorable for low vegetation density (Zhao et al., 2020) and strong freeze-thaw processes, which induced frequent and extreme mass movement and even glacial processes in the east Tibetan Plateau (Heyman et al., 2011; Ou et al., 2014). Those processes resulted in the supply of large amounts of sediment to the river channels and thick valley aggradation. This aggradation phase is consistent with fluvial aggradation around the Tibetan Plateau during the last glacial period (e.g., Ray and Srivastava., 2010; Vandenberghe et al., 2011; Kothyari and Luirei, 2016; Chahal et al., 2019). During deglaciation, monsoon activity became stronger with increased precipitation and denser vegetation cover (Figs. 13C and 13D). This resulted in higher discharges and reduced sediment input, causing river incision and stepped terrace formation from ca. 19 to 11 ka. Thus, episodic weak aggradation resumed during the phase of general river degradation after 19 ka, developing terraces T6 to T3 (Fig. 13). After that, temperature increased with small fluctuations while monsoon precipitation remained relatively stable (Fig. 13). As a result vegetation recovered steadily (Zhao et al., 2020), leading to continued incision. Small fluctuations of precipitation and temperature during the Holocene (Fig. 13), and related changes of vegetation cover (Zhao et al., 2020), may have resulted in episodic interruptions of the general incision and the formation of terraces T2 and T1 at 9 ka and 5 ka, respectively (Fig. 13C). However, internal dynamic factors or episodic tectonic movements cannot be excluded for these Holocene terrace formations (Schumm, 1993).

Fluvial aggradation during the cold LGM and incision during the next deglacial phase occur widely in the surrounding areas. The Lancang River near the study area experienced aggradation at 25–15 ka and incised afterwards (Zhang et al., 2018). In the Himalaya, dry climate conditions during cold periods led to valley filling, while rivers incised and formed terraces during wetter episodes of the late Quaternary (Ray and Srivastava, 2010). In addition, in the Central Kumaun Himalaya, the major phase of Saryu River valley filling was dated between 22 and 14 ka (Kothyari and Luirei, 2016). The Zanskar valley (NW Himalaya) aggraded during the climatic transition from the dry LGM to the wet early Holocene (20–12 ka) followed by rapid incision due to the strong Indian Monsoon (Chahal et al., 2019). The effective moisture availability in the Asian monsoon edge was relatively low during the LGM and high during the Holocene (Fig. 11B). Thus, we hypothesize that glaciation and freezing processes during the LGM in high mountains could provide plenty of sediments to the valley. But, melting of glacier ice (Heyman et al., 2011) and intensified monsoon precipitation since deglaciation (Zhao et al., 2020) might have contributed to increased river discharge and river incision in this high relief area.

The Potential Effects of Extreme Events in the Fluvial Evolution of the Upper Yangtze River

The fact that the presence of mass-flow and slope deposits within the sections does not indicate continuous accumulation, but rather episodic emplacement, especially in the gorge terraces and in the ZMD section (Fig. 10), points to occasional interruption of fluvial processes. In addition, the spatially irregular occurrence of thick gravel deposits of >19–15 ka age (Fig. 5E) points to the local presence of mass-flow and slope processes. Therefore, it is suggested that the latter deposits may be attributed to local occurrence of slope failures or alluvial fans. Considering the combined evidence of local and temporary presence of those deposits suggests localized and temporarily favorable conditions to initiate such slope processes, pointing to rather exceptional or extreme conditions.

In the headwaters of the Yangtze River, the rugged terrain with frequent active faults is episodically vulnerable to extreme mass wasting and strong local orographic precipitation, which may lead to extreme geomorphological processes such as landslides and debris flows (e.g., Bao et al., 2020). This chain of successive extreme events has produced abundant sediments in the valleys, and resulted in repeated short-term blocking of the channel (such as the landslides in Baiyu in October 2018; e.g., Liu et al., 2020), recorded as episodic debris and slope deposits interbedded in the fluvial sediment sequence at ca. 20 ka at the ZMD site in the gorge area.

The multiple cycles of fluvial, debris flows, and colluvial layers at ca. 20 ka at the sites of ZD and ZMD indicate that the change from cold-dry to warm-wet (Fig. 13) at ca. 20 ka, in combination with the delayed re-vegetation of the hillslopes (e.g., Sewell et al., 2015), may have promoted a higher frequency of mass movement and debris flow and resultant blockage of the river (Figs. 8C, 8D, and 10). The same geomorphic processes were also found in the Minjiang and Jinsha rivers at the margin of the Tibetan Plateau (Wang et al., 2007; Chen et al., 2008; Luo et al., 2019; Bao et al., 2020).

The angular boulders at the ZMD site may also indicate earthquakes that shocked and fractured the bedrock at high elevations and triggered a large number of deep-seated bedrock landslides (e.g., Hovius and Stark 2006). Indeed, seven paleo-earthquakes have been identified along the Batang fault (near Yushu) at <22 ka, >14 ka, 14–9.5 ka, 8.0–7.8 ka, >6.7 ka, 4.3–4.0 ka, and <2.7 ka (Huang et al., 2015), which may have produced extreme-event deposits (Fig. 10). Glacier activities could also have formed glacial dams and blocked the river in high mountains (e.g., Korup and Tweed, 2007). But it is debated whether there was a large ice sheet during the late Pleistocene in the central and east Tibetan Plateau, although large numbers of glaciers in high mountains and upstream valleys (such as Queer Shan and Bayan Har Shan) have been suggested (Kuhle, 2004; Stroeven et al., 2009;

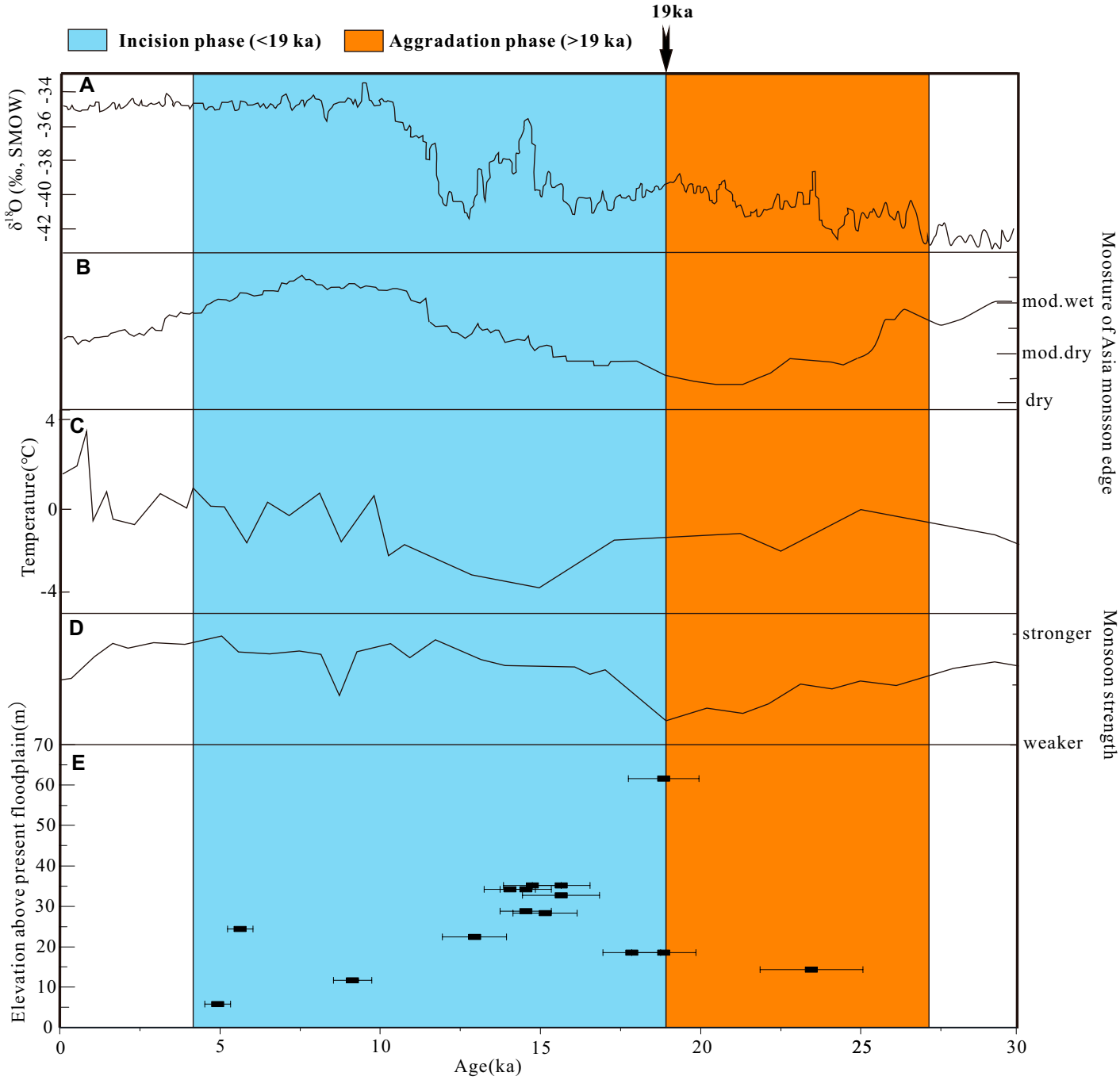

Figure 13. (A) Oxygen isotope records from the Greenland ice sheet (Johnsen et al., 2001). (B) The mean effective moisture from the Asian monsoon edge (Berger and Loutre, 1991). (C and D) are mean annul temperature and monsoon strength in the Zoige basin in the eastern Tibetan Plateau, China (Zhao et al., 2020). (E) Optically stimulated luminescence-ages of valley fill versus elevation above present floodplain for fluvial terraces in this study. SMOW—standard mean ocean water; mod.—moderate.

Shi, 2004). Thus, it remains impossible to exclude the effects of glacial processes on the extreme events. However, these extreme events could have had made significant contributions to the incision of the >1000 m deep canyon in this area and in other regions, an issue deserving of further study.

CONCLUSION

Sedimentary facies analysis with OSL dating of depositional sequences at seven transects along the Upper Yangtze River, differing levels of relative tectonic activity background has allowed the identification of terraces T7–T3 (ca. 19–13 ka), T2 (ca. 9 ka), T1 (ca. 5 ka). The headwaters of the Yangtze River experienced aggradation from the valley base to up to 62 m apf during the LGM; subsequently, there was a change to continuous fluvial incision with episodic lateral erosion and stability. A set of cut-in-fill terraces has formed as a response to

increased climatic conditions with increasing monsoon precipitation and increased vegetation since deglaciation. The relative levels of tectonic activity dominated the distribution pattern and morphologic features of the terraces, while the sediment input from the catchment, directly related to climate change, acted as a primary controlling factor on fluvial processes. In addition, the interbedded debris-flow deposits, fluvial deposits, and colluvial sediments indicate that climate transformation at ca. 20 ka resulted in alternations of fluvial and slope sediments, especially in the gorge area. Emplacement of the deposits was episodic and possibly related to earthquakes, climatic transitions, and/or glacial activities. As a result, ephemeral dams could be created with subsequent sporadic spillovers, outbreaks, and even mega-floods. These geomorphologic processes might have led to extreme fluvial incision and denudation which are characteristic of the geomorphic and landscape evolution of the Tibetan Plateau.

ACKNOWLEDGMENTS

Yan Dai, Junfei Ma, Quanxu Hu, Linman Gao, Xun Yang, Bingling Wang, Wanting Xie, and Zhengchen Li are thanked for their help during the fieldwork. We extend our appreciation to Editor Brad Singer, and two anonymous reviewers for providing thoughtful insights and constructive comments. This research is supported by the National Natural Science Foundation of China (41971005), Second Tibetan Plateau Scientific Expedition Program (STEP) (2019QZKK0205), and the National Key Research and Development Program (grant number 2016YFA0600500).

REFERENCES CITED

Allen, P.A., 2008, From landscapes into geological history: Nature, v. 451, p. 274–276, https://doi.org/10.1038/nature06586.

Bao, Y.D., Zhai, S.J., Chen, J.P., Xu, P.H., Sun, X.H., Zhan, J.W., Zhang, W., and Zhou, X., 2020, The evolution of the Samaoding paleolandslide river blocking event at the upstream reaches of the Jinsha River, Tibetan Plateau: Geomorphology, v. 351, no. 106970, https://doi.org/10.1016/j.geomorph.2019.106970.

Bender, A.M., Amos, C.B., Bierman, P., Rood, D.H., Staisch, L., Kelsey, H., and Sherrod, B., 2016, Differential uplift and incision of the Yakima River terraces, central Washington State: Journal of Geophysical Research. Solid Earth, v. 121, p. 365–384, https://doi.org/10.1002/2015JB012303.

Bender, A.M., Lease, R.O., Haeussler, P.J., Rittenour, T., Corbett, L.B., Bierman, P.R., and Caffee, M.W., 2019, Pace and process of active folding and fluvial incision across the Kantishna Hills anticline, central Alaska: Geophysical Research Letters, v. 46, p. 3235–3244, https://doi.org/10.1029/2018GL081509.

Berger, A., Loutre, M.F., 1991, Insolation values for the climate of the last 10 million years: Quaternary Science Reviews, v, 10, p. 297–317, https://doi.org/10.1016/0277-3791(91)90033-Q.

Bridgland, D.R., and Westaway, R., 2008, Preservation patterns of Late Cenozoic fluvial deposits and their implications: Results from IGCP 449: Quaternary International, v. 189, p. 5–38, https://doi.org/10.1016/j.quaint.2007.08.036.

Chahal, P., Kumar, A., Sharma, C.P., Singhal, S., Sundriyal, Y.P., and Srivastava, P., 2019, Late Pleistocene history of aggradation and incision, provenance and channel connectivity of the Zanskar River, NW Himalaya: Global and Planetary Change, v. 178, p. 110–128, https://doi.org/10.1016/j.gloplacha.2019.04.015.

Chen, J., Dai, F.C., and Yao, X., 2008, Holocene debris-flow deposits and their implications on the climate in the upper Jinsha River valley, China: Geomorphology, v. 93, p. 493–500, https://doi.org/10.1016/j.geomorph.2007.03.011.

Chen, Z.W., Yang, P.X., Li, Z.M., and Li, J.J., 2010, Characteristics of Ms7.1 Yushu earthquake fault and the surface rupture: Quaternary Sciences, v. 30, p. 628–631, https://doi.org/10.3969/j.issn.1001-7410.2010.03.24.

Chug, D., Pathak, A., Indu, J., Jain, S. K., Jain, S. K., Dimri, A. P., Niyogi, D., and Ghosh, S., 2020, Observed evidence for steep rise in the extreme flow of western Himalayan rivers: Geophysical Research Letters, v. 47, no. 15, https://doi.org/10.1029/2020GL087815.

Cook, K.L., Andermann, C., Gimbert, F., Adhikari, B.R., and Hovius, N., 2018, Glacial lake outburst floods as drivers of fluvial erosion in the Himalaya: Science, v. 362, p. 53–57, https://doi.org/10.1126/science.aat4981.

De Paula, B.L.F., and Magalhães, A.P., Jr., 2020, Late quaternary landscape evolution in the Atlantic Plateau (Brazilian highlands): Tectonic and climatic implications of fluvial archives: Earth-Science Reviews, v. 207, no. 103228, https://doi.org/10.1016/j.earscirev.2020.103228.

Deng, Q.D., Zhang, P.Z., Ran, Y.K., Yang, X., Min, W., and Chu, Q.Z., 2003, Basic characteristics of active tectonics of China: Science in China. Series D, Earth Sciences, v. 46, no. 3, p. 356–372.

Duller, G., 2003, Distinguishing quartz and feldspar in single grain luminescence measurements: Radiation Measurements, v. 37, p. 161–165, https://doi.org/10.1016/S1350-4487(02)00170-1.

Duvall, A.R., and Tucker, G.E., 2015, Dynamic ridges and valleys in a strike-slip environment: Journal of Geophysical Research. Earth Surface, v. 120, p. 2016–2026, https://doi.org/10.1002/2015JF003618.

Fan, X.M., Scaringi, G., Korup, O., West, A.J., van Westen, C.J., Tanyas, H., Hovius, N., Hales, T.C., Jibson, R.W., Allstadt, K.E., Zhang, L.M., Evans, S.G., Xu, C., Li, G., Pei, X.J., Xu, Q., and Huang, R.Q., 2019, Earthquake-induced chains of geologic hazards: Patterns, mechanisms, and impacts: Reviews of Geophysics, v. 57, p. 421–503, https://doi.org/10.1029/2018RG000626.

Ferrier, K.L., Huppert, K.L., and Perron, J.T., 2013, Climatic control of bedrock river incision: Nature, v. 496, no. 7444, p. 206–210 https://xs.scihub.ltd/https://doi.org/10.1038/nature11982, https://doi.org/10.1038/nature11982.

Gao, L.M., Wang, X.Y., Yi, S.W., Vandenberghe, J., Gibling, M.R., and Lu, H.Y., 2018, Episodic Sedimentary Evolution of an Alluvial Fan (Huangshui Catchment, NE Tibetan Plateau): Quaternary, v. 1, no. 16, https://doi.org/10.3390/quat1020016.

Guérin, G., Mercier, N., and Adamiec, G., 2011, Dose-rate conversion factors: Update: Ancient TL, v. 29, p. 5–8.

Handwerger, A.L., Fielding, E.J., Huang, M.H., Bennett, G.L., Liang, C., and Schulz, W.H., 2019, Widespread initiation, reactivation, and acceleration of landslides in the northern California Coast Ranges due to extreme rainfall: Journal of Geophysical Research. Earth Surface, v. 124, p. 1782–1797, https://doi.org/10.1029/2019JF005035.

Henck, A.C., Huntington, K.W., Stone, J.O., Montgomery, D.R., and Hallet, B., 2011, Spatial controls on erosion in the Three Rivers Region, southeastern Tibet and southwestern China: Earth and Planetary Science Letters, v. 303, p. 71–83, https://doi.org/10.1016/j.epsl.2010.12.038.

Hewitt, K., Clague, J.J., and Orwin, J.F., 2008, Legacies of catastrophic rock slope failures in mountain landscapes: Earth-Science Reviews, v. 87, p. 1–38, https://doi.org/10.1016/j.earscirev.2007.10.002.

Heyman, J., Stroeven, A.P., Caffee, M.W., Hättestrand, C., Harbor, J.M., Li, Y.K., Alexanderson, H., Zhou, L.P., and Hubbard, A., 2011, Palaeoglaciology of Bayan Har Shan, NE Tibet Plateau: Exposure ages reveal a missing LGM expansion: Quaternary Science Reviews, v. 30, p. 1988–2001, https://doi.org/10.1016/j.quascirev.2011.05.002.

Hovius, N., and Stark, C.P., 2006, Landslide-driven erosion and topographic evolution of active mountain belts, *in* Evans, S.G., Mugnozza, G.S., Strom, A., and Hermanns, R.L., eds., Landslides From Massive Rock Slope Failure: Berlin, Germany, Springer, p. 573–590, https://doi.org/10.1007/978-1-4020-4037-5_30.

Huang, X.M., Du, Y., He, Z.T., Ma, B.Q., and Xie, F.R., 2015, Late Pleistocene–Holocene paleoseismology of the Batang fault (central Tibet plateau, China): Geomorphology, v. 239, p. 127–141, https://doi.org/10.1016/j.geomorph.2015.03.026.

Johnsen, S.J., Dahl-Jensen, D., Gundestrup, N., Steffensen, J.P., Clausen, H.B., Miller, H., Masson-Delmotte, V., Sveinbjörnsdottir, A.E., and White, J., 2001, Oxygen isotope and palaeotemperature records from six Greenland ice-core stations: Camp Century, Dye-3, GRIP, GISP2: Renland and NorthGRIP: Journal of Quaternary Science, v. 16, p. 299–307, https://doi.org/10.1002/jqs.622.

Kirby, E., Whipple, K.X., Tang, W., and Chen, Z., 2003, Distribution of active rock uplift along the eastern margin of the Tibetan Plateau: Inferences from bedrock channel longitudinal profiles: Journal of Geophysical Research. Solid Earth, v. 108, no. B4, https://doi.org/10.1029/2001JB000861.

Kong, P., Na, C.G., Fink, D., Zhao, X.T., and Xiao, W., 2009, Moraine dam related to late Quaternary glaciation in the Yulong Mountains, southwest China, and impacts on the Jinsha River: Quaternary Science Reviews, v. 28, p. 3224–3235, https://doi.org/10.1016/j.quascirev.2009.08.005.

Korup, O., and Montgomery, D.R., 2008, Tibetan plateau river incision inhibited by glacial stabilization of the Tsangpo gorge: Nature, v. 455, p. 786–789, https://doi.org/10.1038/nature07322.

Korup, O., and Tweed, F., 2007, Ice, moraine, and landslide dams in mountainous terrain: Quaternary Science Reviews, v. 26, p. 3406–3422, https://doi.org/10.1016/j.quascirev.2007.10.012.

Korup, O., Montgomery, D.R., and Hewitt, K., 2010a, Glacier and landslide feedbacks to topographic relief in the Himalayan syntaxes: Proceedings of the National Academy of Sciences of the United States of America, v. 107, p. 5317–5322, https://doi.org/10.1073/pnas.0907531107.

Korup, O., Densmore, A.L., and Schlunegger, F., 2010b, The role of landslides in mountain range evolution: Geomorphology, v. 120, p. 77–90, https://doi.org/10.1016/j.geomorph.2009.09.017.

Kothyari, G.C., and Luirei, K., 2016, Late Quaternary tectonic landforms and fluvial aggradation in the Saryu River valley: Central Kumaun Himalaya: Geomorphology, v. 268, p. 159–176, https://doi.org/10.1016/j.geomorph.2016.06.010.

Kuhle, M., 2004, The high glacial (last ice age and LGM) ice cover in High and Central Asia, *in* Ehlers, J., and Gibbard, P.L., eds., Quaternary Glaciations Extent and Chronology: Part III: South America, Asia, Africa, Australasia, Antarctica: Elsevier, Developments in Quaternary Sciences Series, v. 2, p. 175–199, https://doi.org/10.1016/S1571-0866(04)80123-4.

Li, Y.J., Armitage, S.J., Stevens, T., and Meng, X.M., 2018, Alluvial fan aggradation /incision history of the eastern Tibetan plateau margin and implications for debris flow/debris-charged flood hazard: Geomorphology, v. 318, p. 203–216, https://doi.org/10.1016/j.geomorph.2018.06.016.

Liu, W.M., Lai, Z.P., Hu, K.H., Ge, Y.G., Cui, P., Zhang, X.G., and Liu, F., 2015, Age and extent of a giant glacial-dammed lake at Yarlung Tsangpo gorge in the Tibetan Plateau: Geomorphology, v. 246, p. 370–376, https://doi.org/10.1016/j.geomorph.2015.06.034.

Liu, W.M., Hu, K.H., Carling, P.A., Lai, Z.P., Cheng, T., and Xu, Y.L., 2018, The establishment and influence of Baimakou paleo-dam in an upstream reach of the Yangtze River, southeastern margin of the Tibetan Plateau: Geomorphology, v. 321, p. 167–173, https://doi.org/10.1016/j.geomorph.2018.08.028.

Liu, W.M., Carling, P.A., Hu, K.H., Wang, H., Zhou, Z., Zhou, L.Q., Liu, D.Z., Lai, Z.P., and Zhang, X.B., 2019, Outburst floods in China: A review: Earth-Science Reviews, v. 197, no. 102895, https://doi.org/10.1016/j.earscirev.2019.102895.

Liu, W., Ju, N.P., Zhang, Z., Chen, Z., and He, S.M., 2020, Simulating the process of the Jinshajiang landslide-caused disaster chain in October 2018: Bulletin of Engineering Geology and the Environment, v. 79, p. 2189–2199, https://doi.org/10.1007/s10064-019-01717-6.

Luo, X.K., Yin, Z.Q., and Yang, L.W., 2019, Preliminary analysis on the development characteristics of river terraces and their relationship with ancient landslides in the reaches of Minjiang River [in Chinese]: Quaternary Sciences, v. 2, p. 391–398, https://doi.org/10.11928/j.issn.1001-7410.2019.02.11.

Maddy, D., Bridgland, D.R., and Green, C.P., 2000, Crustal uplift in southern England: Evidence from the river terrace records: Geomorphology, v. 33, p. 167–181, https://doi.org/10.1016/S0169-555X(99)00120-8.

Mejdahl, V., 1979, Thermoluminescence Dating: Beta-dose attenuation in quartz grains: Archaeometry, v. 21, p. 61–79, https://doi.org/10.1111/j.1475-4754.1979.tb00241.x.

Miall, A.D., 1996, The Geology of Fluvial Deposits: Sedimentary Facies, Basin Analysis, and Petroleum Geology: Berlin-Heidelberg, Germany, Springer, 582 p.

Molnar, P., and Houseman, G.A., 2013, Rayleigh-Taylor instability, lithospheric dynamics, surface topography at convergent mountain belts, and gravity anomalies: Journal of Geophysical Research. Solid Earth, v. 118, no. 5, p. 2544–2557, https://doi.org/10.1002/jgrb.50203.

Molnar, P., England, P., and Martinod, J., 1993, Mantle dynamics, uplift of the Tibetan Plateau, and the Indian monsoon: Reviews of Geophysics, v. 31, p. 357–396, https://doi.org/10.1029/93RG02030.

Murray, A.S., and Wintle, A.G., 2000, Luminescence dating of quartz using an improved single-aliquot regenerative dose protocol: Radiation Measurements, v. 32, p. 57–73, https://doi.org/10.1016/S1350-4487(99)00253-X.

Murray, A.S., and Wintle, A.G., 2003, The single aliquot regenerative dose protocol: Potential for improvements in reliability: Radiation Measurements, v. 37, p. 377–381, https://doi.org/10.1016/S1350-4487(03)00053-2.

Nie, J.S., Ruetenik, G., Gallagher, K., Hoke, G., Garzione, C.N., Wang, W.T., Stockli, D., Hu, X.F., Wang, Z., Wang, Y., Stevens, T., Danišík, M., and Liu, S.P., 2018, Rapid incision of the Mekong River in the middle Miocene linked to monsoonal precipitation: Nature Geoscience, v. 11, p. 944–948, https://doi.org/10.1038/s41561-018-0244-z.

Ou, X.J., Lai, Z.P., Zhou, S.Z., and Zeng, L.H., 2014, Timing of glacier fluctuations and trigger mechanisms in eastern Qinghai-Tibetan plateau during the late quaternary: Quaternary Research, v. 81, p. 464–475, https://doi.org/10.1016/j.yqres.2013.09.007.

Ray, Y., and Srivastava, P., 2010, Widespread aggradation in the mountainous catchment of the Alaknanda-Ganga River System: Timescales and implications to Hinterland-foreland relationships: Quaternary Science Reviews, v. 29, p. 2238–2260, https://doi.org/10.1016/j.quascirev.2010.05.023.

Rhoads, B., 2020, River Dynamics: Geomorphology to Support Management: Cambridge, UK, Cambridge University Press, https://doi.org/10.1017/9781108164108.

Schanz, S.A., Montgomery, D.R., Collins, B.D., and Duvall, A.R., 2018, Multiple paths to straths: A review and reassessment of terrace genesis: Geomorphology, v. 312, p. 12–23, https://doi.org/10.1016/j.geomorph.2018.03.028.

Schumm, S.A., 1993, River Response to baselevel Change: Implications for Sequence Stratigraphy: The Journal of Geology, v. 101, p. 279–294, https://doi.org/10.1086/648221.

Sewell, R.J., Parry, S., Millis, S.W., Wang, N., Rieser, U., and DeWitt, R., 2015, Dating of debris flow fan complexes from Lantau Island, Hong Kong, China: The potential relationship between landslide activity and climate change: Geomorphology, v. 248, p. 205–227, https://doi.org/10.1016/j.geomorph.2015.07.041.

Shi, Y.F., 2004, The emergence and abandonment of the ice sheet hypothesis over the Qinghal-Xizang Plateau during the ice age [in Chinese]: Quaternary Sciences, v. 24, p. 10–18, https://doi.org/10.3321/j.issn:1001-7410.2004.01.002.

Sømme, T.O., and Jackson, C.A.-L., 2013, Source-to-sink analysis of ancient sedimentary systems using a subsurface case study from the Møre-Trøndel ag area of southern Norway: Part 2-sediment dispersal and forcing mechanisms: Basin Research, v. 25, p. 512–531, https://doi.org/10.1111/bre.12014.

Srivastava, P., Tripathi, J.K., Islam, R., and Jaiswal, M.K., 2008, Fashion and phases of late Pleistocene aggradation and incision in the Alaknanda River Valley, western Himalaya, India: Quaternary Research, v. 70, p. 68–80, https://doi.org/10.1016/j.yqres.2008.03.009.

Stokes, M., Mather, A.E., Rodes, A., Kearsey, S.H., and Lewin, S., 2018, Anatomy, age and origin of an intramontane top basin surface (Sorbas Basin, Betic Cordillera, SE Spain): Quaternary, v. 1, no. 15, https://doi.org/10.3390/quat1020015.

Stroeven, A.P., Hättestrand, C., Heyman, J., Harbor, J., Li, Y., Zhou, L., Caffee, M.W., Alexanderson, H., Kleman, J., Ma, H., and Liu, G., 2009, Landscape analysis of the Huang He headwaters, NE Tibetan Plateau: Patterns of glacial and fluvial erosion: Geomorphology, v. 103, p. 212–226, https://doi.org/10.1016/j.geomorph.2008.04.024.

Tao, Y.L., Xiong, J.G., Zhang, H.P., Chang, H., and Li, L.Y., 2020, Climate-driven formation of fluvial terraces across the Tibetan Plateau science 200 kya: A review: Quaternary Science Reviews, v. 237, no. 106303, https://doi.org/10.1016/j.quascirev.2020.106303.

Tapponnier, P., Xu, Z.Q., Roger, F., Meyer, B., Arnaud, N., Wittlinger, G., and Yang, J.S., 2001, Oblique stepwise rise and growth of the Tibet Plateau: Science, v. 294, p. 1671–1677, https://doi.org/10.1126/science.105978.

Taylor, M., and Yin, A., 2009, Active structures of the Himalayan-Tibetan orogen and their relationships to earthquake distribution, contemporary strain field, and Cenozoic volcanism: Geosphere, v. 5, no. 3, p. 199–214, https://doi.org/10.1130/GES00217.1.

Vandenberghe, J., 2015, River terraces as a response to climatic forcing: formation processes, sedimentary characteristics and sites for human occupation: Quaternary International, v. 370, p. 3–11, https://doi.org/10.1016/j.quaint.2014.05.046.

Vandenberghe, J., Wang, X.Y., and Lu, H.Y., 2011, Differential impact of small-scaled tectonic movements on fluvial morphology and sedimentology (the Huang Shui catchment, NE Tibet Plateau): Geomorphology, v. 134, p. 171–185, https://doi.org/10.1016/j.geomorph.2011.06.020.

Vandenberghe, J., Kasse, C., Popov, D., Markovic, S.B., Vandenberghe, D., Bohncke, S., and Gabris, G., 2018, Specifying the external impact on fluvial lowland evolution: The last glacial Tisza (Tisa) catchment in Hungary and Serbia: Quaternary, v. 1, no. 14, https://doi.org/10.3390/quat1020014.

Wang, L.S., Wang, X.Q., Xu, X.N., and Cui, J., 2007, What happened on the upstream of Minjiang River in Sichuan Province 20000 years ago [in Chinese]: Earth Science Frontiers, v. 14, no. 4, p. 189–196.

Wang, S.F., Fan, C., Wang, G., and Wang, E.C., 2008, Late Cenozoic deformation along the northwestern continuation of the Xianshuihe fault system, Eastern Tibetan Plateau: Geological Society of America Bulletin, v. 120, p. 312–327, https://doi.org/10.1130/B25833.1.

Wang, X.Y., Lu, H.Y., Vandenberghe, J., Chen, Z.Y., and Li, L.P., 2010, Distribution and Forming Model of Fluvial Terrace in the Huangshui Catchment and its Tectonic Indication: Acta Geologica Sinica, v. 84, p. 415–423, https://doi.org/10.1111/j.1755-6724.2010.00155.x.

Wang, X.Y., Van Balen, R., Yi, S.W., Vandenberghe, J., and Lu, H.Y., 2014, Differential tectonic movements in the confluence area of the Huang Shui and Huang He rivers (Yellow River), NE Tibetan Plateau, as inferred from fluvial terrace positions: Boreas, v. 43, p. 469–484, https://doi.org/10.1111/bor.12054.

Wang, X.Y., Vandenberghe, J., Yi, S.W., Van Balen, R., and Lu, H.Y., 2015, Climate-dependent fluvial architecture and processes on a suborbital timescale in areas of rapid tectonic uplift: an example from the NE Tibetan Plateau: Global and Planetary Change, v. 133, p. 318–329, https://doi.org/10.1016/j.gloplacha.2015.09.009.

Wen, X.Z., Huang, S.M., and Jiang, Z.X., 1985, Neotectonic characteristics and seismic risk assessment of the Ganzi-Yushu fault zone [in Chinese]: Dizhen Dizhi, v. 7, p. 23–32.

Wen, X.Z., Xu, X.W., Zheng, R.Z., Xie, Y.Q., and Wan, C., 2003, The average slip rate of Ganzi-Yushu fault and the fragmentation of modern earthquake [in Chinese]: Science China(D), v. 33, p. 199–208, https://doi.org/10.3321/j.issn:1006-9267.2003.z1.022.

Whipple, K.X., Kirby, E., and Brocklehurst, S.H., 1999, Geomorphic limits to climate-induced increases in topographic relief: Nature, v. 401, p. 39–43, https://doi.org/10.1038/43375.

Wu, Q.L., Zhao, Z.J., Liu, L., Granger, D.E., Wang, H., Cohen, D.J., Wu, X.H., Ye, M.L., Bar-Yosef, O., Liu, B., Zhang, J., Zhang, P.Z., Yuan, D.Y., Qi, W.Y., Cai, L.H., and Bai, S.B., 2016, Outburst flood at 1920 BCE supports historicity of China's Great Flood and the Xia dynasty: Science, v. 353, p. 579–582, https://doi.org/10.1126/science.aaf0842.

Wu, Z.H., Zhao, X.T., Fan, T.Y., Ye, P.S., Tong, Y.B., and Yang, Z.Y., 2012, Active faults and seismologic characteristics along the Dali-Ruili railway in western Yunnan Province [in Chinese]: Geological Bulletin of China, v. 31, p. 191–217.

Zhang, G.H., Shan, X.J., Delouis, B., Qu, C.Y., Balestra, J., Li, Z.H., Liu, Y.H., and Zhang, G.F., 2013, Rupture history of the 2010 Ms 7.1 Yushu earthquake by joint inversion of teleseismic data and InSAR measurements: Tectonophysics, v. 584, p. 129–137, https://doi.org/10.1016/j.tecto.2012.03.024.

Zhang, J.Y., Liu-Zeng, J., Scherler, D., Yin, A., Wang, W., Tang, M.Y., and Li, Z.F., 2018, Spatiotemporal variation of late Quaternary river incision rates in southeast Tibet, constrained by dating fluvial terraces: Lithosphere, v. 10, p. 662–676, https://doi.org/10.1130/L686.1.

Zhao, Y., Tzedakis, P.C., Li, Q., Qin, F., Cui, Q.Y., Liang, C., Birks, H.B., Liu, Y.L., Zhang, Z.Y., Ge, J.Y., Zhao, H., Felde, V.A., Deng, C.L., Cia, M.T., Li, H., Ren, W.H., Wei, H.C., Yang, H.F., Zhang, J.W., Yu, Z.C., and Guo, Z.T., 2020, Evolution of vegetation and climate variability on the Tibet Plateau over the past 1.74 million years: Science Advances, v. 6, no. 6193, https://doi.org/10.1126/sciadv.aay6193.

Zhou, R.J., Ma, S.H., and Cai, C.S., 1996, Late Quaternary active features of the Ganzi–Yushu fault zone [in Chinese]: Earthquake Research in China, v. 12, p. 250–260.

Zhou, R.J., Wen, X.Z., Cai, C.X., and Ma, S.H., 1997, Recent earthquakes and assessment of seismic tendency on the Ganzi-Yushu fault zone [in Chinses]: Dizhen Dizhi, v. 19, p. 115–124.

Zhou, R.J., Li, Y., Liang, M.J., Xu, X.W., He, Y.L., Wang, S.Y., Ma, C., and Liu, Y.F., 2014, Determination of mean recurrence interval of large earthquakes on the Garzê-Yushu Fault (Dengke Segment) on the eastern margin of the Qinghai-Tibetan Plateau: Quaternary International, v. 333, p. 179–187, https://doi.org/10.1016/j.quaint.2013.11.010.

Science Editor: Brad S. Singer
Associate Editor: Emmanuel Gabet

Manuscript Received 22 November 2020
Revised Manuscript Received 20 February 2021
Manuscript Accepted 4 April 2021

Printed in the USA